

A STUDY OF REVERSED BENDING FATIGUE  
IN THE NICKEL-COPPER ALLOY,  
MONEL K-500

By

GREGORY WAYNE HENDERSON

Bachelor of Science

University of Connecticut

Storrs, Connecticut

1973

Submitted to the Faculty of the Graduate College  
of the Oklahoma State University  
in partial fulfillment of the requirements  
for the Degree of  
MASTER OF SCIENCE  
December, 1979

Thesis  
1979  
H4965s  
cop. 2



A STUDY OF REVERSED BENDING FATIGUE  
IN THE NICKEL-COPPER ALLOY,  
MONEL K-500

Thesis Approved:

*B. E. Fine*

Thesis Adviser

*DKM Laughlin*

*R. G. Murray*

*Norman N. Durham*

Dean of the Graduate College

1042367

## ACKNOWLEDGMENTS

I would like to express my appreciation to Dr. C. E. Price, the thesis adviser, for his continuing instruction and encouragement throughout all segments of this work. Appreciation is also extended to Dr. R. G. Murray for his related support as a committee member. I extend a special note of thanks to Dr. D. K. McLaughlin for his advice concerning graduate study and also for serving as a committee member.

The School of Mechanical and Aerospace Engineering at Oklahoma State University provided a research assistantship and the necessary equipment. The Huntington Alloys Company supplied the materials.

Finally, I am sincerely grateful to my wife, Marion, and my parents, Mr. and Mrs. Herschel Henderson, for their understanding and support.

## TABLE OF CONTENTS

Chapter	Page
I. INTRODUCTION . . . . .	1
Objectives . . . . .	2
II. EXPERIMENTAL PROCEDURES . . . . .	4
Approach . . . . .	4
The Material . . . . .	5
Specimen Geometry . . . . .	7
Specimen Preparation . . . . .	10
Fatigue Testing . . . . .	11
III. EXPERIMENTAL RESULTS . . . . .	14
IV. DISCUSSION . . . . .	68
V. CONCLUSIONS . . . . .	75
A SELECTED BIBLIOGRAPHY . . . . .	76
APPENDIX . . . . .	78

LIST OF TABLES

Table	Page
I. Chemical Composition . . . . .	6
II. Physical Constants . . . . .	6
III. Mechanical Properties . . . . .	15
IV. Summary of Surface Hardness Profiles . . . . .	39

## LIST OF FIGURES

Figure	Page
1. Specimen Geometry of the Original Design (a), Improved Design (b), and Fatigue Testing Configuration (c) . . . . .	9
2. Budd Reversed Bending Fatigue Machine, Model VSP-150 with Strain Controlled Operation . . . . .	13
3. Fatigue Life As a Function of Bending Displacement for Three Heat Treatments . . . . .	17
4. Legend for Surface Hardness Profiles . . . . .	19
5. Surface Hardness Profile of Solution Heat Treated Specimen Number 31, $N_f = 5400$ . . . . .	21
6. Surface Hardness Profile of Overaged Specimen Number 27, $N_f = 5565$ . . . . .	23
7. Surface Hardness Profile of Optimum Aged Specimen Number 18, $N_f = 29,700$ . . . . .	25
8. Surface Hardness Profile of Solution Heat Treated Specimen Number 8, $N_f = 1,123,400$ . . . . .	28
9. Surface Hardness Profile of Overaged Specimen Number 37, $N_f = 3,261,900$ . . . . .	30
10. Surface Hardness Profile of Optimum Aged Specimen Number 22, Side "A", $N_f = 24,263,100$ . . . . .	32
11. Surface Hardness Profile of Optimum Aged Specimen Number 22, Side "B", $N_f = 24,263,100$ . . . . .	34
12. Superposition of Surface Hardness Profiles for Two Solution Heat Treated Specimens; Number 31, $N_f = 5,400$ , and Number 8, $N_f = 1,123,400$ . . . . .	36
13. Superposition of Surface Hardness Profiles for Two Overaged Specimens; Number 27, $N_f = 5,565$ and Number 37, $N_f = 3,261,900$ . . . . .	38
14. Optical Microscope Photograph of Massive Slip and Secondary Cracking at the Fracture Edge . . . . .	41

Figure	Page
15. The Same Specimen as Shown in Figure 14 with Evidence of Slip Extending Back 28 mm to the Clamping Point . . . . .	41
16. Localized Slip at Fracture Edge for HCF . . . . .	43
17. Transverse Slip Band Gradient with a Higher Concentration of Slip Markings Appearing at Gauge Length Edges . . . . .	43
18. Triplex Slip Illustrating the Multiplicity of Slip Systems Activated in LCF . . . . .	45
19. Duplex Slip with Pronounced Vertical Slip Bands Oriented Parallel to the Fracture Edge . . . . .	45
20. Longitudinal and Transverse Slip Band Cracking Occurring Adjacent to Intergranular Cracking . . . . .	48
21. The Same Specimen as Shown in Figure 20 with Typical Mixed Mode Cracking . . . . .	48
22. Fatigued and Then Etched Surface Marked by Existence of Inclusions, Slip Lines, and Cracks . . . . .	50
23. Intergranular Cracking Through Inclusions Precipitated at Grain Boundaries . . . . .	50
24. Intergranular Crack Adjacent to an Inclusion . . . . .	52
25. Group of Slip Bands Adjacent to Primary Fracture in HCF . . . . .	54
26. SEM Photograph of the Primary Fracture of Figure 25 . . . . .	54
27. Extrusions and Cracks Emanating from the Prominent Slip Bands of Figures 25 and 26 . . . . .	56
28. Slip in Two Directions with Some Extrusions . . . . .	56
29. Mixed Mode Cracking in Areas of Concentrated Slip . . . . .	58
30. Intergranular Cracking Situated Near Regions of Dense Slip Band Formation . . . . .	58
31. Local Accommodation of Stress is Achieved by Slip Band Formation and Intergranular Cracking . . . . .	60
32. A Completely Isolated Grain Exhibiting Ductile Tearing Through Continuous Slip Lines and Twin Boundaries . . . . .	60
33. Duplex Slip on Both Sides of a Single Slip Band Crack That Terminates at a Cracked Grain Boundary . . . . .	62

Figure	Page
34. Crack at a Second Phase Particle . . . . .	62
35. Considerable Amount of Secondary Cracking Amidst Coarse LCF Striations . . . . .	64
36. Secondary Cracking Associated with Fine HCF Striations in the Central Region of the Fracture Surface . . . . .	67
37. Stage I to Stage II Crack Propagation Transition . . . . .	67
38. Representative Strain Gradients for Monel K-500 and Nickel 200 as a Function of Depth . . . . .	71
39. Geometry of Specimen Shown in "Maximum Height Upward" Position . . . . .	81
40. Geometry of Specimen Shown in "Minimum Height Downward" Position . . . . .	83
41. Bending Displacement as a Function of Crank Offset Setting . .	86

## LIST OF SYMBOLS

a	crack length
D	bending displacement
H <sub>v</sub>	Vickers hardness
MHD	minimum height downward
MHU	maximum height upward
n	number of cycles
N <sub>f</sub>	cycles to failure
OA	optimum aged
OVA	overaged
S	crank offset setting
SHT	solution heat treated
t	thickness
γ'	(Ni <sub>3</sub> Al, Ni <sub>3</sub> Ti) phase
σ	applied stress

## CHAPTER I

### INTRODUCTION

Fatigue and/or corrosion accounts for eighty to ninety percent of all engineering material failures according to several estimates. The recent crash of a commercial DC-10 jetliner is a vivid example of the tragic consequences that can arise due to fatigue. Recognizing its importance, engineers and scientists have sought to find ways of eliminating or reducing fatigue. Unfortunately, in many cases the result has been overdesign of the product. The current energy situation requires that such design philosophy should not be practiced. In fact, in areas such as transportation, emphasis has been placed on fuel efficient designs with minimum weight. Recently, there has been a heightened awareness regarding the catastrophic nature of fatigue in the ever increasing number of product liability suits.

The fundamental prerequisite for metal fatigue is the existence of a cyclic applied plastic strain. In either case, a surface crack develops usually at a stress concentration or metallurgical defect and then continues to grow. This first step is known as crack initiation and is immediately followed by stage I crack propagation. Stage I propagation involves the progress of the crack along crystallographic planes from the surface of the material to a depth of perhaps 10  $\mu\text{m}$  to 200  $\mu\text{m}$ . At this point, a transition occurs and stage II crack propagation takes over, traversing the remaining thickness of the material

along non-crystallographic planes. It is during this stage of development that striations, the precursor of final fast fracture, are formed.

Fatigue is particularly insidious with respect to crack growth rate per cycle ( $n$ ). This is often expressed as a function of crack length ( $a$ ) and applied stress ( $\sigma$ ) where the exponents ( $m$ ) and ( $n$ ) are constants (9):

$$\frac{da}{dn} \propto \sigma^m a^n$$

This equation predicts slow initial development of a crack, but a final rapid increase in growth rate, often without warning.

In light of the continuing uncertainties relevant to fatigue, it was hoped that this study might enhance the understanding of the fatigue process in certain specific alloys. In addition, this understanding might contribute towards the successful design of new alloys, and perhaps to the fundamental aspects of fatigue itself.

#### Objectives

The two principal objectives that were established for this study are presented here. First, investigate the progression of fatigue damage in Monel K-500<sup>1</sup> as a function of bending displacement and thermal treatment. Second, compare the surface and fracture zone changes stemming from fatigue in Monel K-500 with acquired data on nickel.

In connection with Monel K-500, some specific objectives were

---

<sup>1</sup>Monel is a registered trademark of the International Nickel Company.

to examine:

1. The effects that selected heat treatments have on fatigue behavior.
2. The extent to which surface zone hardening occurs.
3. If slip morphology varies with heat treatment and bending displacement.
4. What the slip morphology is in contrast to that of nickel.
5. If a distinct stage I to stage II crack propagation transition occurs and its location.
6. If pronounced slip bands are cracked.
7. The influence that stacking fault energy has on the relative proportions of planar and wavy slip.

## CHAPTER II

### EXPERIMENTAL PROCEDURES

#### Approach

To study effectively the fatigue behavior of Monel K-500, five stages of work were carried out:

1. Compression testing to determine monotonic strength properties. The information obtained at this point served as a guide in the planning of subsequent experimental procedures.
2. Fatigue testing in fully reversed, pure bending. Solution heat treated, optimum aged, and overaged specimens were cycled to failure with lives varying from  $10^3$  to  $10^8$  cycles.
3. Measuring hardness profiles over the gauge length of selected specimens. Microhardness testing was employed to reflect only the surface hardness changes associated with fatigue.
4. Observation of fatigued specimens with the optical microscope. Photographs were taken along the gauge length in conjunction with Normarski interference contrast equipment.
5. Observation of fatigue specimens with the scanning electron microscope. Both the gauge length and primary fracture surface were observed.

## The Material

Monel K-500 is a commercially available nickel copper alloy known especially for its superior corrosion resistance. Some applications include sheathing fasteners for offshore drilling platforms, pump shafts and impellers, and oil well drilling components. The material was received in the form of cold-rolled and solution heat-treated sheet, 1.5 mm thick. All specimens were machined from the same sheet, heat number M9673K. Relevant properties are given in Tables I and II.

Specific reasons for the alloy selection are as follows:

1. Monel consists primarily of nickel and copper, both of which have been studied in commercially pure and alloyed forms. It was anticipated that nearly any fatigue research involving Monel would be complementary to these two important metals.
2. Monel K-500, in contrast to certain other Monels, has the capacity to be heat treated. The precipitation of the sub-microscopic  $\gamma'$  phase ( $\text{Ni}_3\text{Al}$ ,  $\text{Ni}_3\text{Ti}$ ) allows for high strength and ductility with minimal lattice distortion. Thus in fatigue testing, two important independent variables were implemented, metallurgical condition and bending displacement.
3. Monel K-500 has a face-centered cubic lattice structure. Microscopic observations are enhanced by the more pronounced slip occurring within the grains.
4. The strain hardening capacity of Monel K-500 is a function of metallurgical condition (17). Therefore, the three different heat treatments utilized serve as a basis for comparison of hardness profiles and microscopic observations.

TABLE I  
CHEMICAL COMPOSITION

---

Element	Heat Number M9673K (weight per cent)
Nickel	64.36
Copper	30.46
Carbon	0.17
Manganese	0.60
Iron	0.75
Sulfur	0.005
Silicon	0.12
Aluminum	2.99
Titanium	0.52

---

TABLE II  
PHYSICAL CONSTANTS

---

Specific Gravity	8.46
Melting Temperature, °C	1320
Modulus of Elasticity, GPa	180
Poisson's Ratio	0.32

---

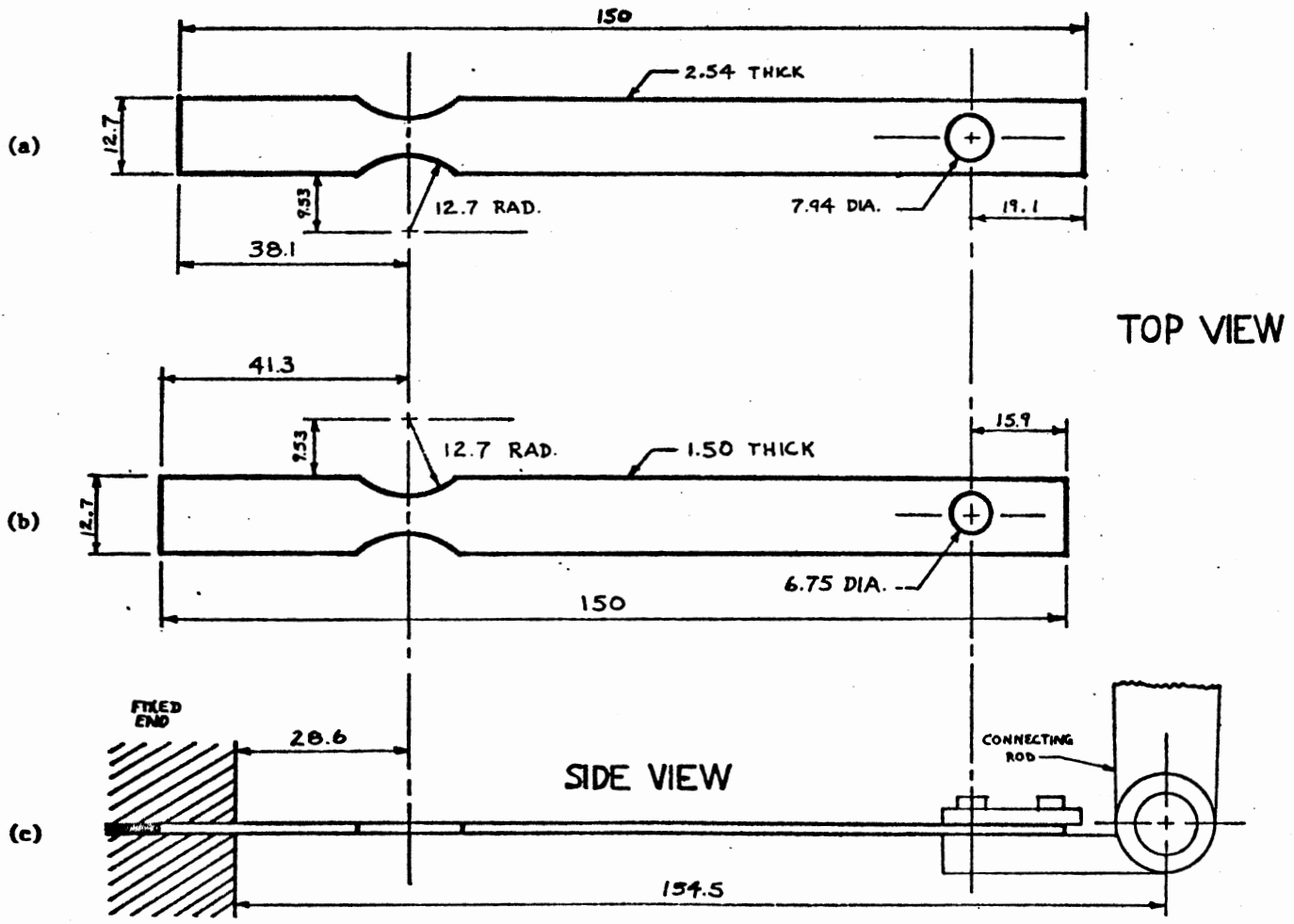
5. The solution heat treated and optimum aged specimens, representing the softest and hardest thermal treatments respectively, were well within the range of the Leitz micro-hardness tester. Two indenter weights were used satisfactorily, 500 and 100 grams.
6. The excellent corrosion resistance of Monel K-500 was not a prerequisite, but was beneficial for laboratory fatigue testing. Relative to other more corrosive metals, the environmental ill effects are substantially less.

#### Specimen Geometry

The basic specimen configuration chosen was chiefly a result of previous work done with nickel by Kreiner (13) and Fila (3) at Oklahoma State University. Early intentions with Monel were to retain the original geometry so as to encourage meaningful comparisons of data. In contrast to nickel specimens, Monel exhibited much higher strength and was approximately half as thick. This required a higher strain amplitude for an equivalent fatigue life. Preliminary fatigue tests with Monel exhibited fretting at the fixed end of the specimen and asymmetrical fracture "seams" along the fracture surface. Consequently, the specimen geometry was altered as shown in Figure 1. Material was removed from the connecting red clamp end and added to the fixed end of all specimens. It is important to note from this figure that the effective moment arm and gauge length dimensions were unchanged, thus the analysis of fatigue data could still be extended to the nickel.

The notched specimen configuration was selected since it renders increased reproducibility, with fatigue failures consistently occurring

Figure 1. Specimen Geometry of the Original Design (a), Improved Design (b), and Fatigue Testing Configuration (c)



in the same location. The gauge length incorporates a 12.7 mm radius which avoids an unnecessarily severe stress concentration. Furthermore, the smooth gradient of strain produces a correspondingly gradual change in surface hardness which is more successfully monitored with micro-hardness measurements. The overall dimensions were fixed because of size limitations imposed by the stage of the scanning electron microscope. Also the compactness of size allowed all specimens to be machined from the same sheet of material.

### Specimen Preparation

Monel K-500 produces a stable oxide film when heated due to the aluminum and titanium alloying additions (10). To minimize oxidation, all specimens were highly polished before thermal treatment. Specimens were mechanically polished with silicon carbide abrasive papers to a 600 grit finish followed by 5 micron and 1 micron rotary polishing respectively. Electropolishing was accomplished at a current density of  $0.80 \text{ amp/cm}^2$  for 30 seconds using nickel foil cathodes. The electrolyte was comprised of a solution of two-thirds methanol to one-third concentrated hydrochloric acid. Finished specimens were stored in dessicators.

Three groups of specimens were vacuum furnace heat-treated according to the following procedure:

1. Solution heat treatment at  $930^{\circ}\text{C}$  for 10 minutes. Water quench with 2% methanol by volume to suppress oxide formation.
2. Optimum age to precipitate the  $\gamma'$  phase. Soak at  $590^{\circ}\text{C}$  for 16 hr, furnace cool to  $540^{\circ}\text{C}$ , hold for 6 hr, furnace cool to  $480^{\circ}\text{C}$ , hold for 8 hr, furnace cool to room temperature (1).

3. Overage at 730°C for 72 hr, furnace cool.

All specimens were Rockwell hardness tested at a non-critical point to ensure uniform response to heat treatment. The solution heat treated and overaged specimens tended to oxidize very lightly in spite of precautions taken. An additional 1 micron rotary polish and 30 sec. electropolish successfully eliminated the oxide with no detectable cold work effects, such as a change in microhardness values.

Microscopic observation was occasionally improved by electrolytic etching to emphasize grain boundaries. With the same electrolyte described for electropolishing, a current density of  $2.5 \times 10^{-3}$  amp/cm<sup>2</sup> was applied for a duration of 5 seconds.

#### Fatigue Testing

All specimens were cycled to failure with a Budd VSP-150 reversed bending fatigue machine, Figure 2. This particular model is designed such that fatigue is strain controlled, with bending displacement confined to fixed limits. Bending is fully reversed and symmetric such that any particular location within the volume of the specimen is subjected to equal amounts of compression and tension. The frequency selected was 35 Hz while the ambient temperature remained at approximately 25°C.

Figure 2. Budd Reversed Bending Fatigue Machine, Model VSP-150 with  
Strain Controlled Operation



## CHAPTER III

### EXPERIMENTAL RESULTS

The monotonic strength properties of Monel K-500 are presented in Table III and originated primarily from tests conducted by Price (17). Specimens were machined from 12.7 mm diameter round stock and tested in compression. Of particular importance were the three strain hardening exponents calculated for each of the heat treatments discussed earlier in experimental procedures.

For low cycle fatigue (LCF), which is often designated as less than  $5 \times 10^4$  cycles, optimum aged specimens of Figure 3 displayed superior life. Solution heat treated and overaged specimens exhibited significantly less life. In the high cycle fatigue (HCF) regime, or greater than  $1 \times 10^6$  cycles, fatigue life was much less dependent upon heat treatment. The overaged curve was bounded by the solution heat treated curve for low cycle fatigue and perhaps bounded more by the optimum aged curve for high cycle fatigue.

Surface hardness profiles for low cycle fatigue of selected specimens are presented in Figures 5 through 7. It was seen that the surface hardness varied measurably with the solution heat treated specimen for both indenter weights. The overaged specimen exhibited a more gradual hardening trend towards the fracture zone. The optimum aged specimen did not seem to show a hardness change at all.

Hardness trends for high cycle fatigue were similar, but less

TABLE III  
MECHANICAL PROPERTIES

Material Condition	Tensile Strength (MPa)	Yield Strength 0.2% Offset (MPa)	Hardness Rockwell	Strain Hardening Coefficient (MPa)	Strain Hardening Exponent
Cold-rolled, Solution heat-treated	670	360	79B	1240	0.35
Optimum aged	1100	760	32C	1500	0.16
Overaged	-	-	83B	970	0.30

Figure 3. Fatigue Life As a Function of Bending Displacement for Three Heat Treatments

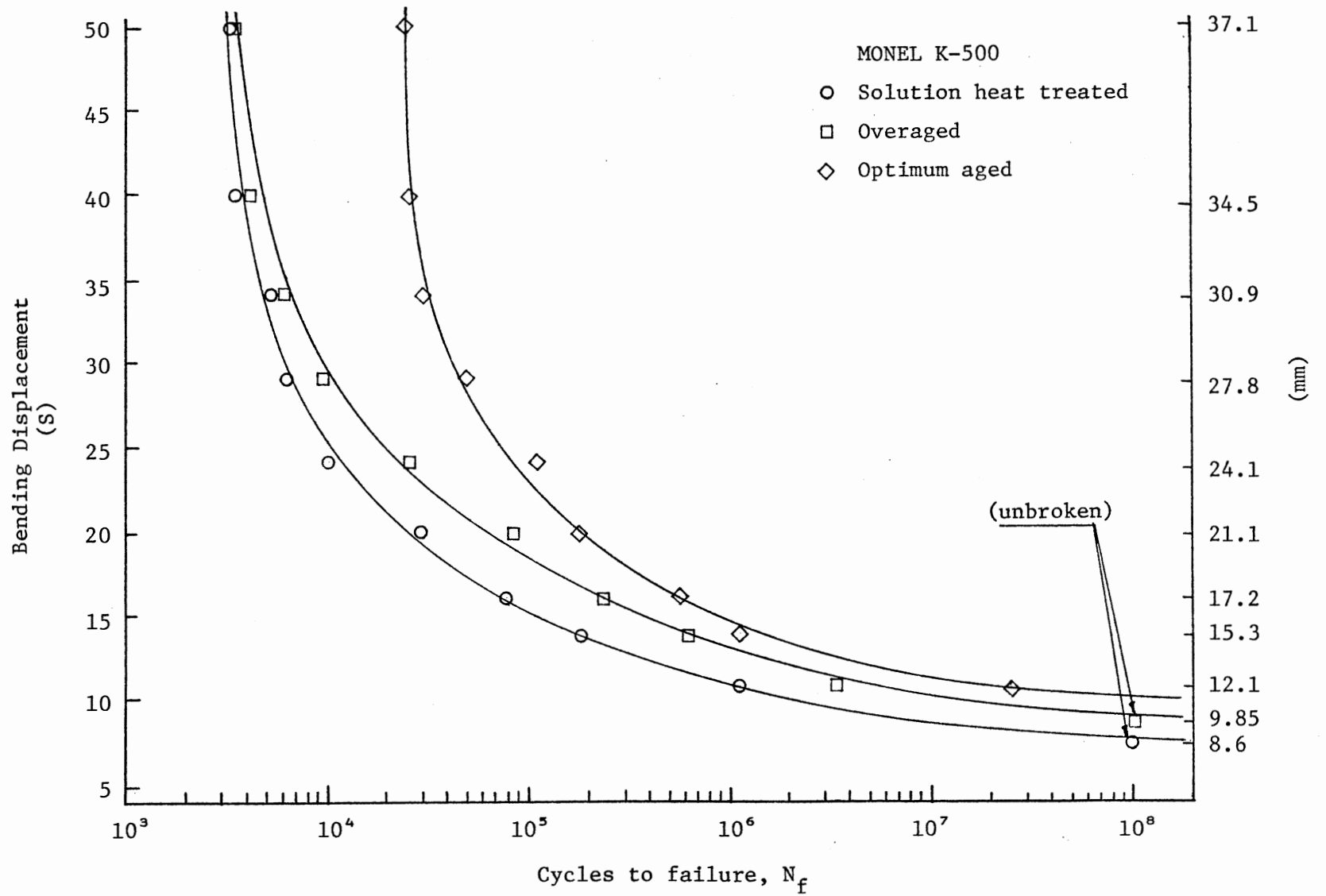
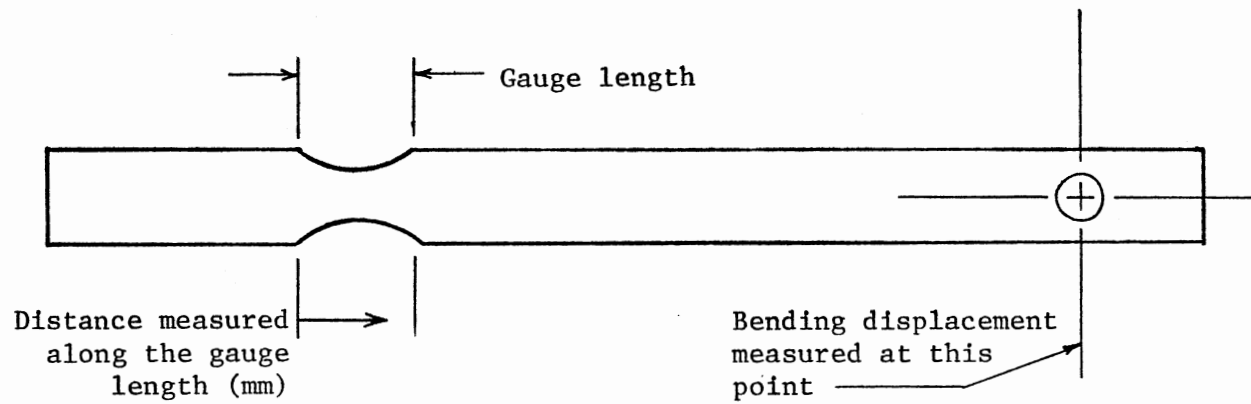


Figure 4. Legend for Surface Hardness Profiles



Indenter weights used with Leitz microhardness tester: 500 g, 100 g  
D = bending displacement

Figure 5. Surface Hardness Profile of Solution Heat Treated Specimen  
Number 31,  $N_f = 5400$

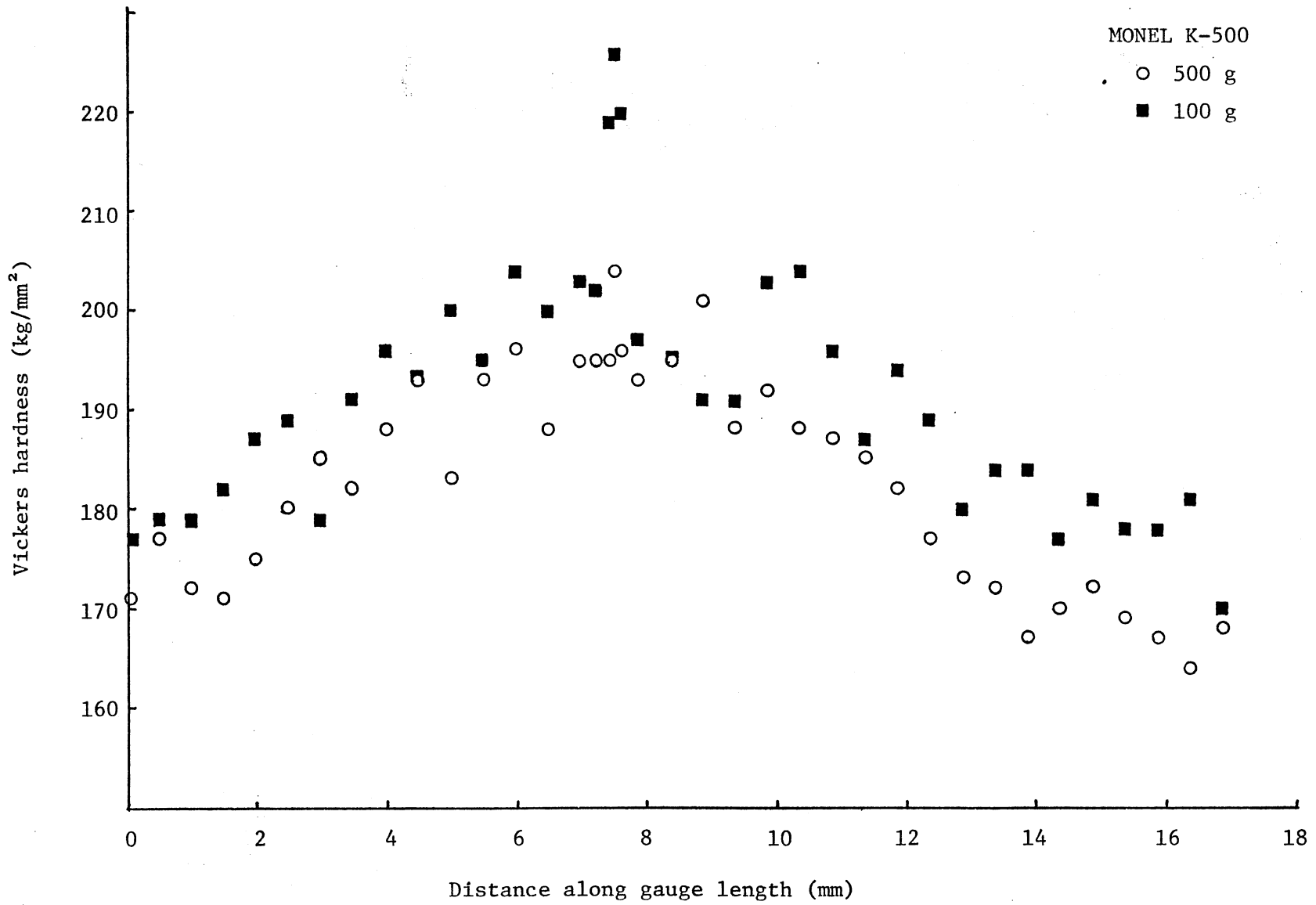


Figure 6. Surface Hardness Profile of Overaged Specimen Number 27,  
 $N_f = 5565$

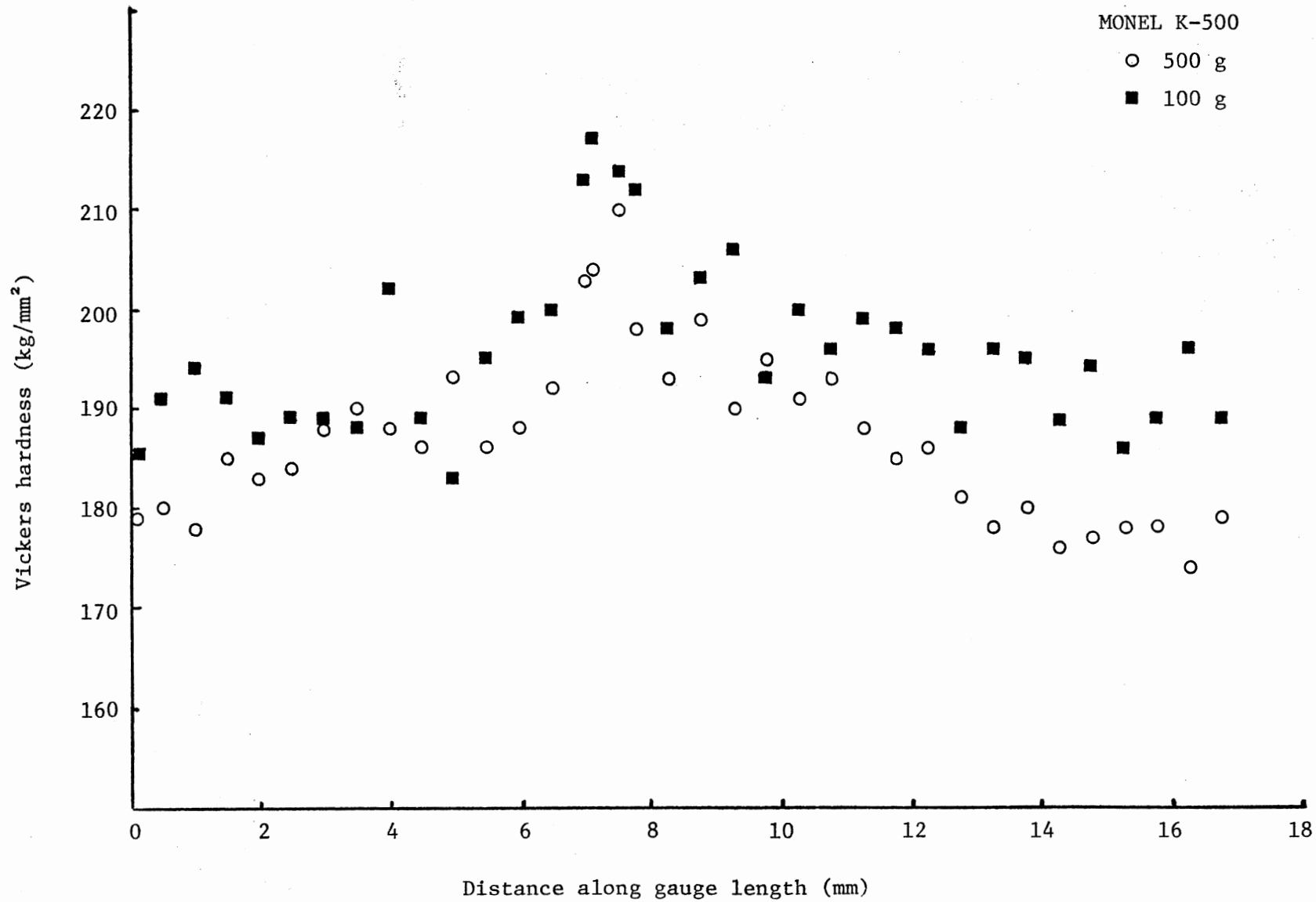
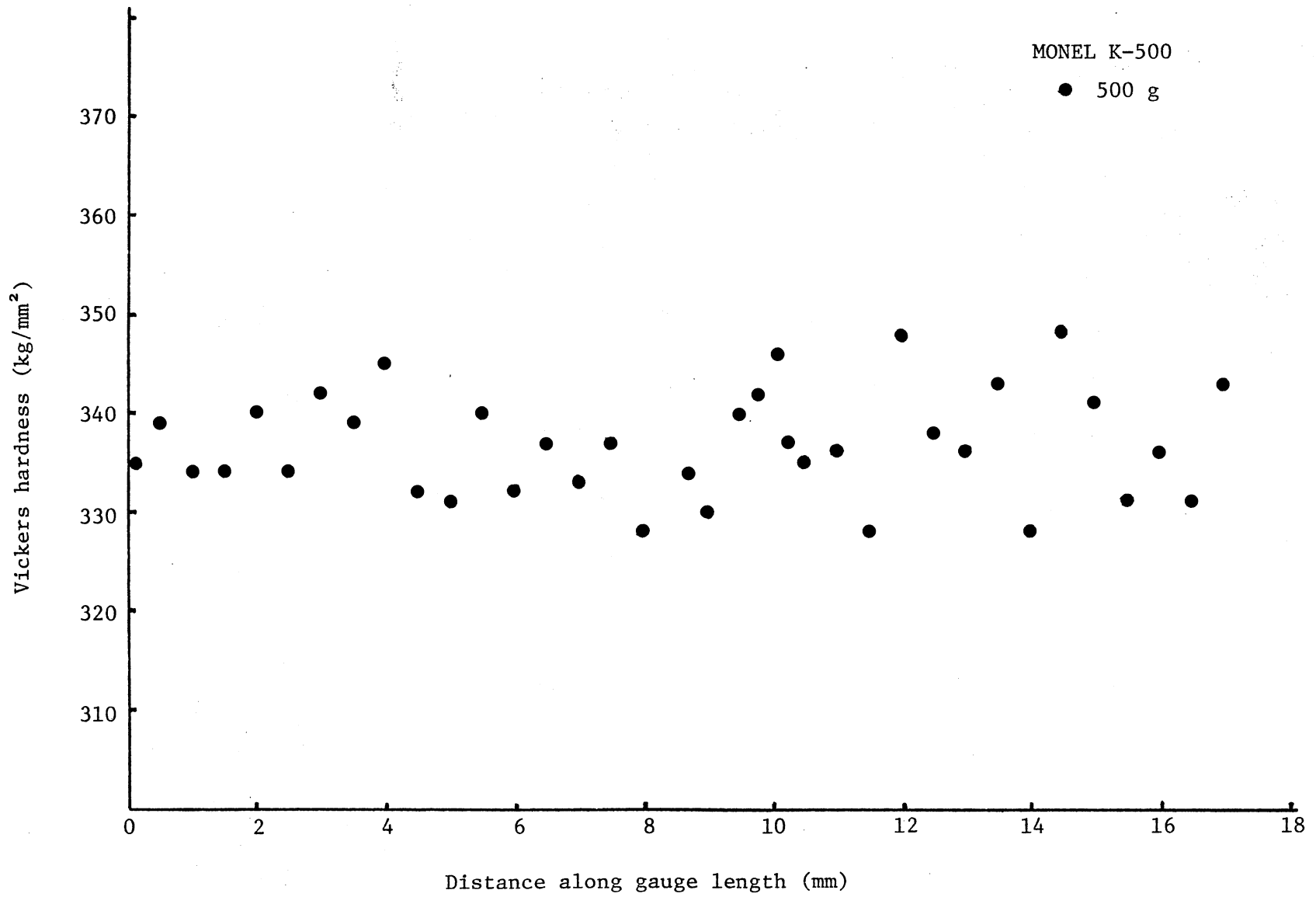


Figure 7. Surface Hardness Profile of Optimum Aged Specimen Number 18,  
 $N_f = 29,700$



dramatic, Figures 8 through 11. Further illustration of this is seen in Figures 12 and 13 where graphic superpositions of solution heat treated and overaged specimens are portrayed, respectively. Specimen 22, side "A", showed perhaps a slight softening in the vicinity of fracture. Note that specimen 22, side "B" did not harden in this same region. With the exception of the optimum aged heat treatment, specimens were characterized by conspicuously high surface hardness values immediately adjacent to the fracture zone. A summary of features regarding surface hardness profiles is included in Table IV.

Figures 14 and 16 indicate clearly that the extent of fatigue damage varied as a function of heat treatment and bending displacement. For each heat treatment, fatigue damage was seen to decrease with increasing life. Heat treatment appeared to have a greater effect than cycles to failure. The density of slip and cracking was observed to be roughly proportional to the magnitude of the strain hardening exponent. Solution heat treated specimens with the relatively high strain hardening exponent suffered the greatest amount of damage, Figures 14 and 15. Optimum aged specimens with the lowest strain hardening exponent suffered the least, Figure 16. While the quantity of fatigue damage seen at the surface varied with heat treatment and bending displacement, the important characteristics remained essentially the same.

Other features included the transverse gradient of slip density, Figure 17. At the edges of the gauge length a relatively greater concentration of massive slip bands were produced. Multiple slip directions were most often seen at the higher bending displacements, Figures 18 and 19.

Figure 8. Surface Hardness Profile of Solution Heat Treated Specimen  
Number 8,  $N_f = 1,123,400$

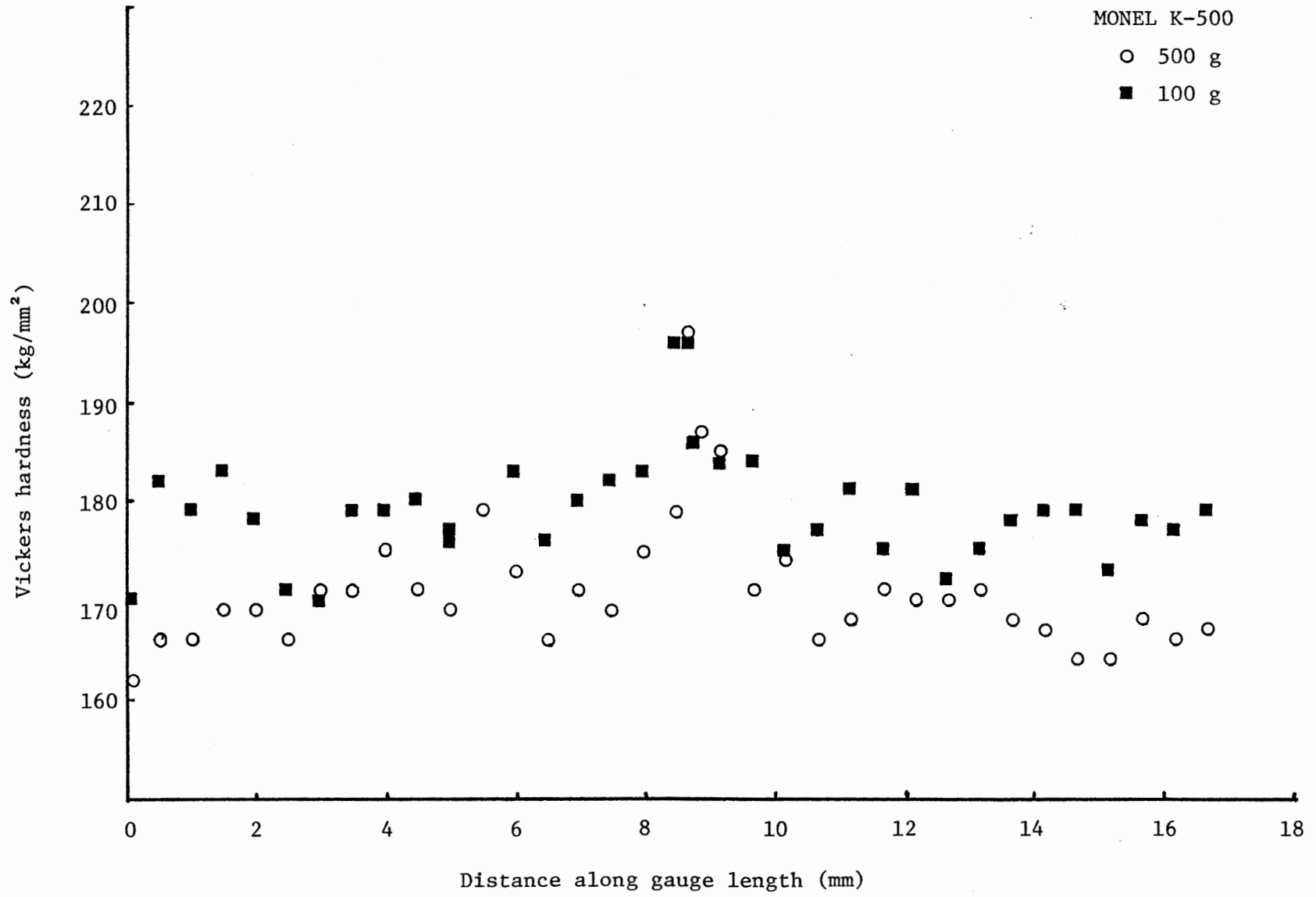


Figure 9. Surface Hardness Profile of Overaged Specimen Number 37,  
 $N_f = 3,261,900$

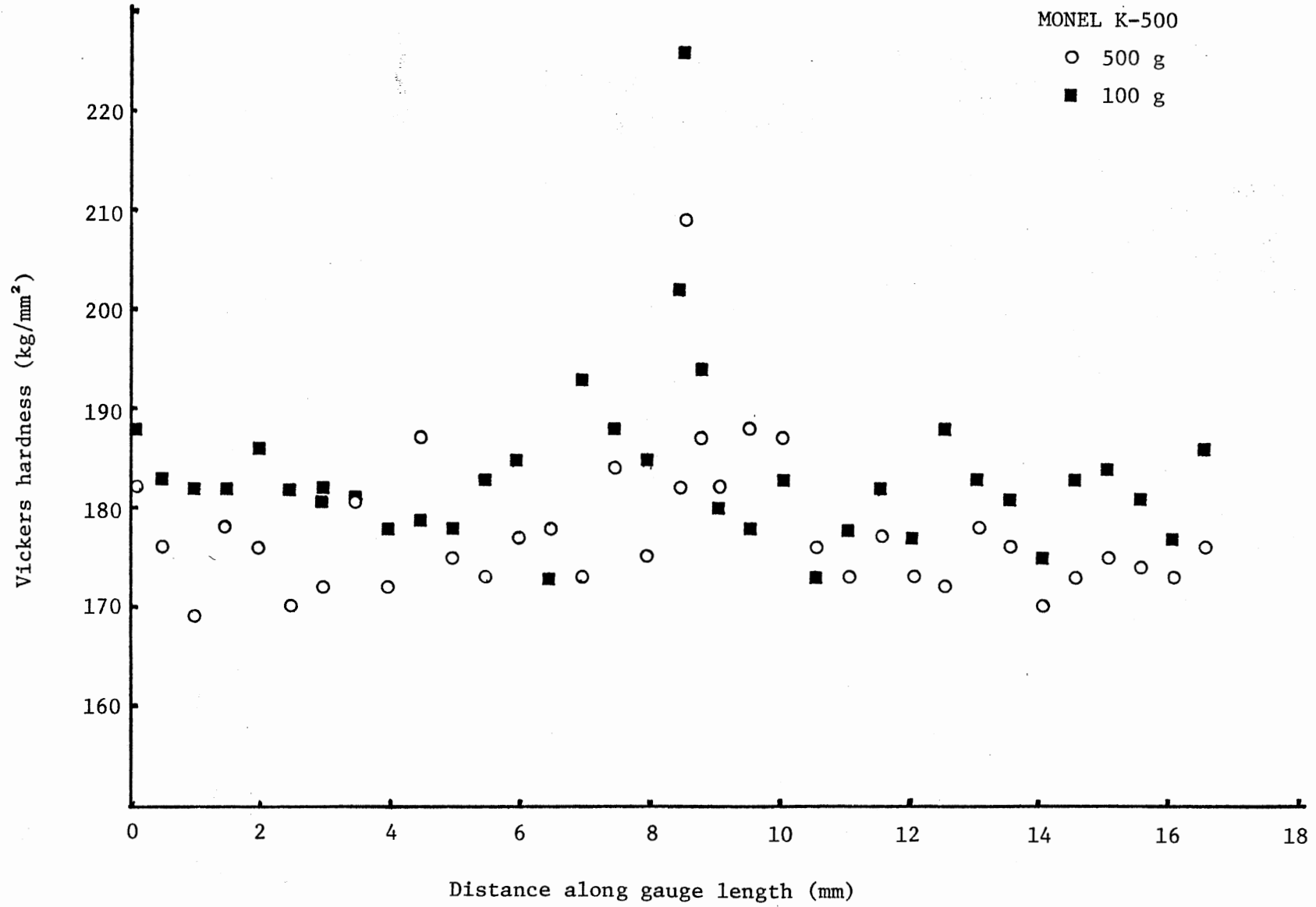


Figure 10. Surface Hardness Profile of Optimum Aged Specimen Number  
22, Side "A",  $N_f = 24,263,100$

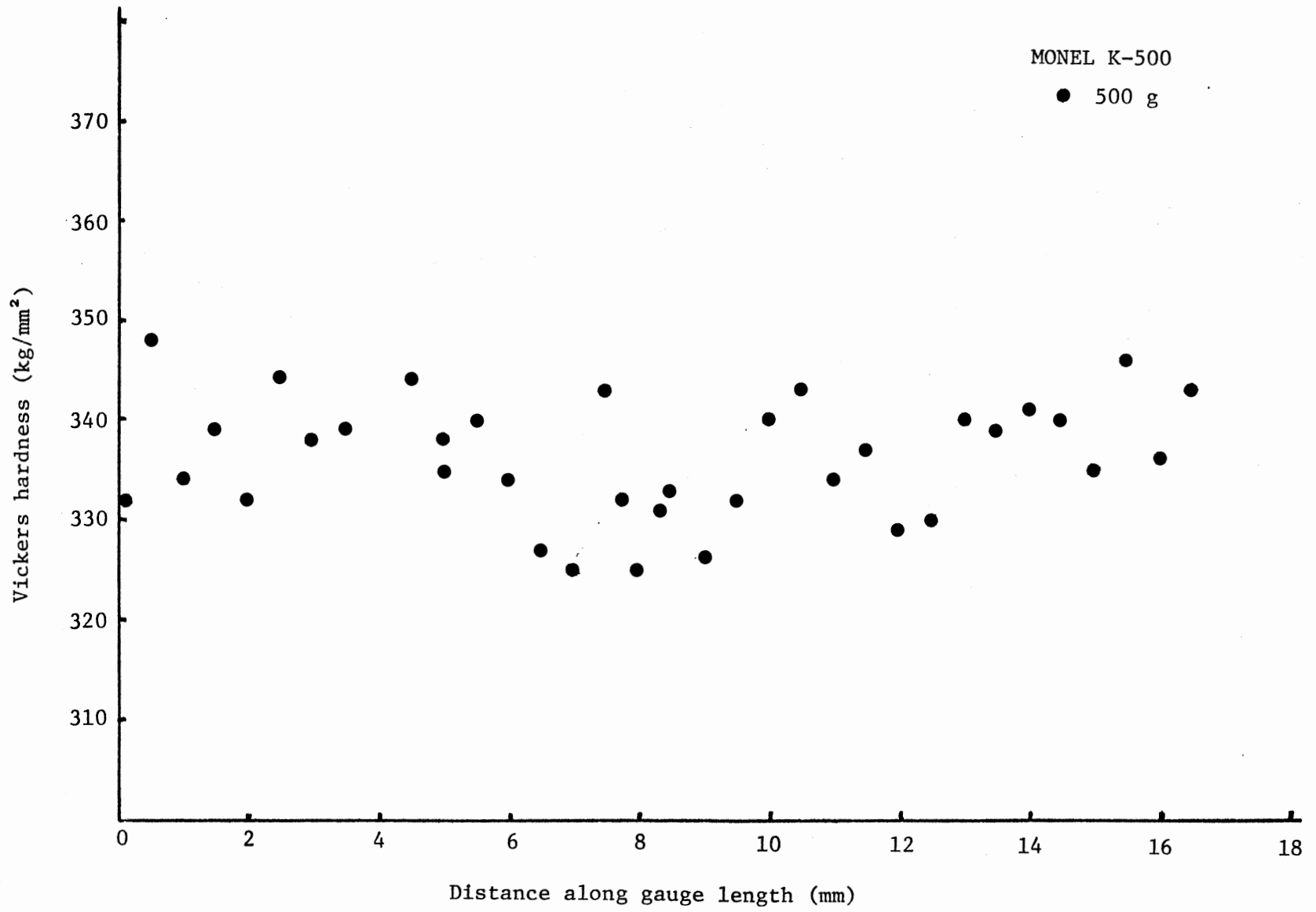


Figure 11. Surface Hardness Profile of Optimum Aged Specimen Number  
22, Side "B",  $N_f = 24,263,100$

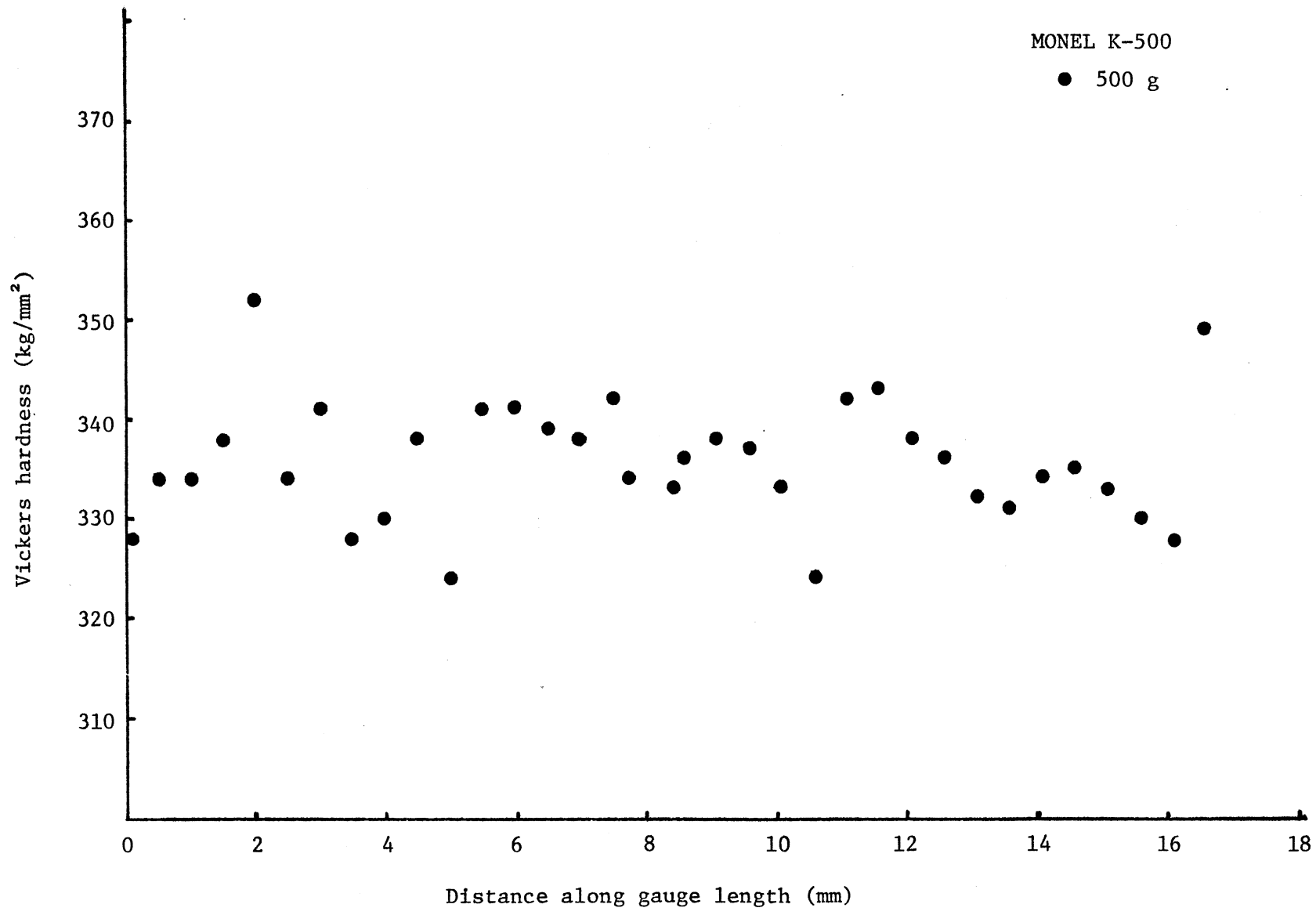


Figure 12. Superposition of Surface Hardness Profiles for Two Solution Heat Treated Specimens; Number 31,  $N_f = 5,400$ , and Number 8,  $N_f = 1,123,400$

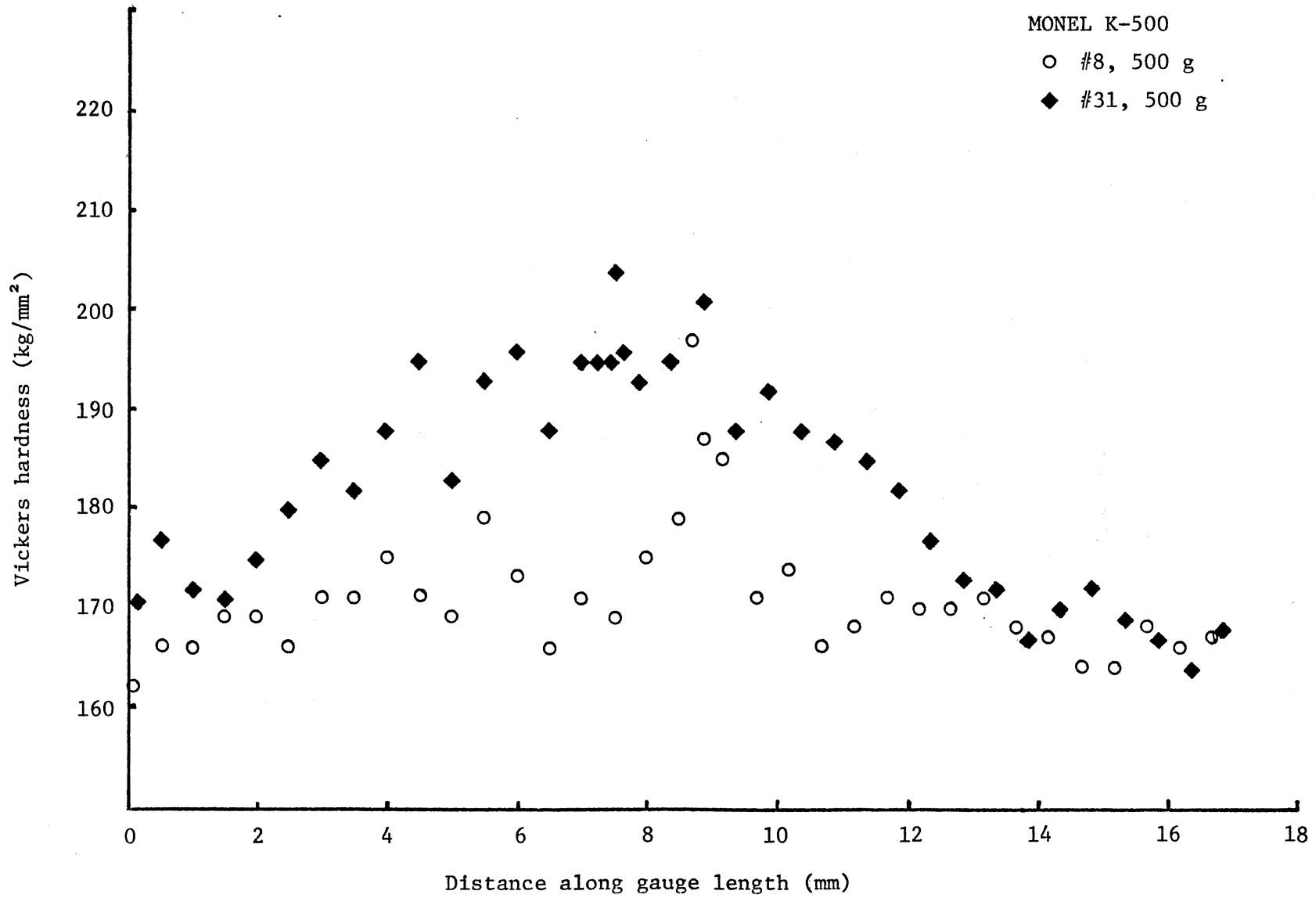


Figure 13. Superposition of Surface Hardness Profiles for Two Overaged Specimens; Number 27,  $N_f = 5,565$  and Number 37,  $N_f = 3,261,900$

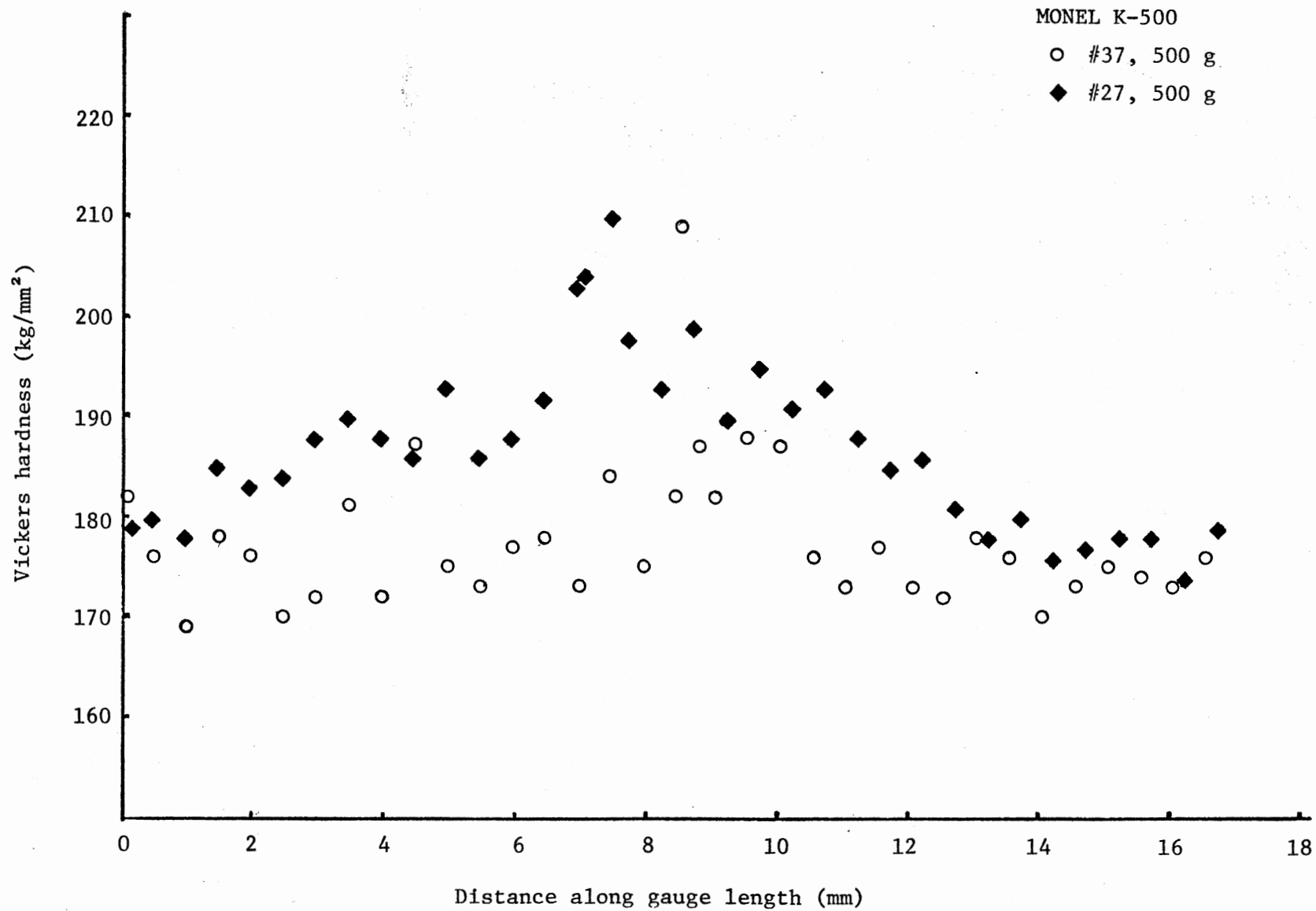


TABLE IV  
SUMMARY OF SURFACE HARDNESS PROFILES

	SHT		OVA		OA
	500 g	100 g	500 g	100 g	500 g
Average minimum hardness (kg/mm <sup>2</sup> )	160	165	170	170	340
Average maximum hardness (kg/mm <sup>2</sup> )	205	225	205	215	340
Hardness at first signs of slip (kg/mm <sup>2</sup> )	175	170	185	195	340

Figure 14. Optical Microscope Photograph of Massive Slip and Secondary Cracking at the Fracture Edge. Morphology is typical of high amplitude testing for soft material in LCF. Specimen number 32, SHT D = 37.1 mm,  $N_f = 3480$  (x 98).

Figure 15. The Same Specimen as Shown in Figure 14 with Evidence of Slip Extending Back 28 mm to the Clamping Point. The vertical scratch at right serves to align the vise jaws. Specimen number 32, SHT, D = 37.1 mm,  $N_f = 3480$  (x 385).

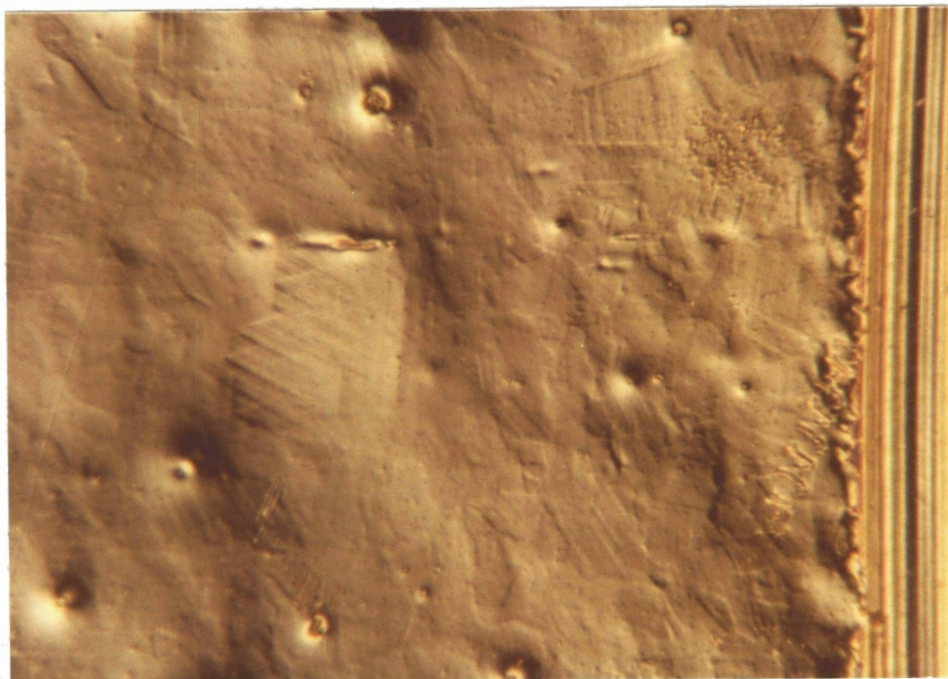


Figure 16. Localized Slip at Fracture Edge for HCF. Slip band density is low and extends back approximately 0.4 mm. Specimen number 22, OA, D = 12.2 mm,  $N_f = 24,263,000$  (x 98).

Figure 17. Transverse Slip Band Gradient with a Higher Concentration of Slip Markings Appearing at Gauge Length Edges. Specimen number 9, SHT, D = 15.3 mm,  $N_f = 253,400$  (x 195).

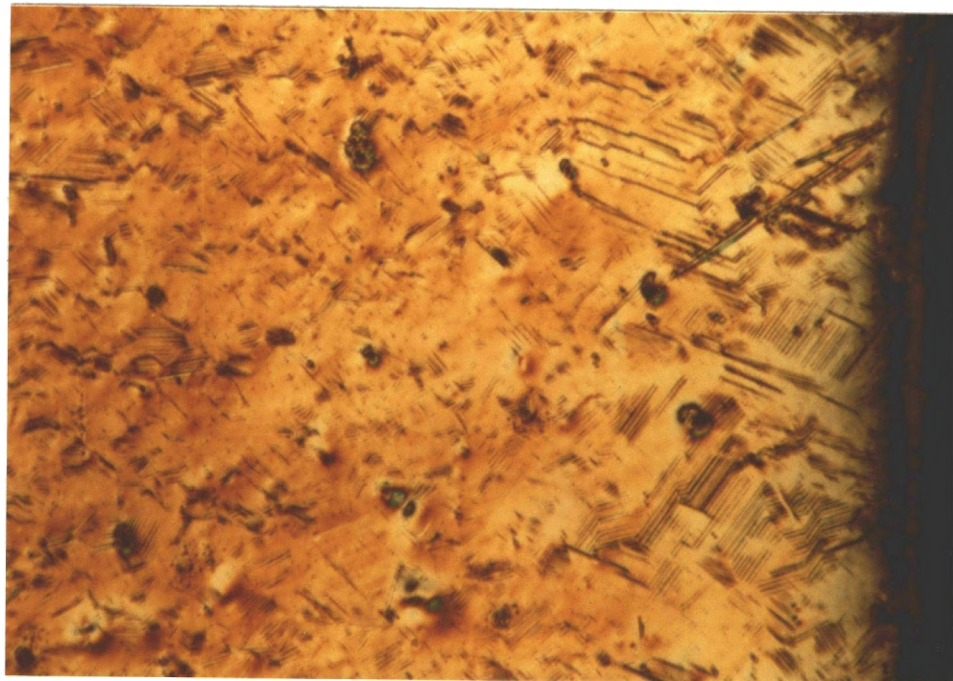
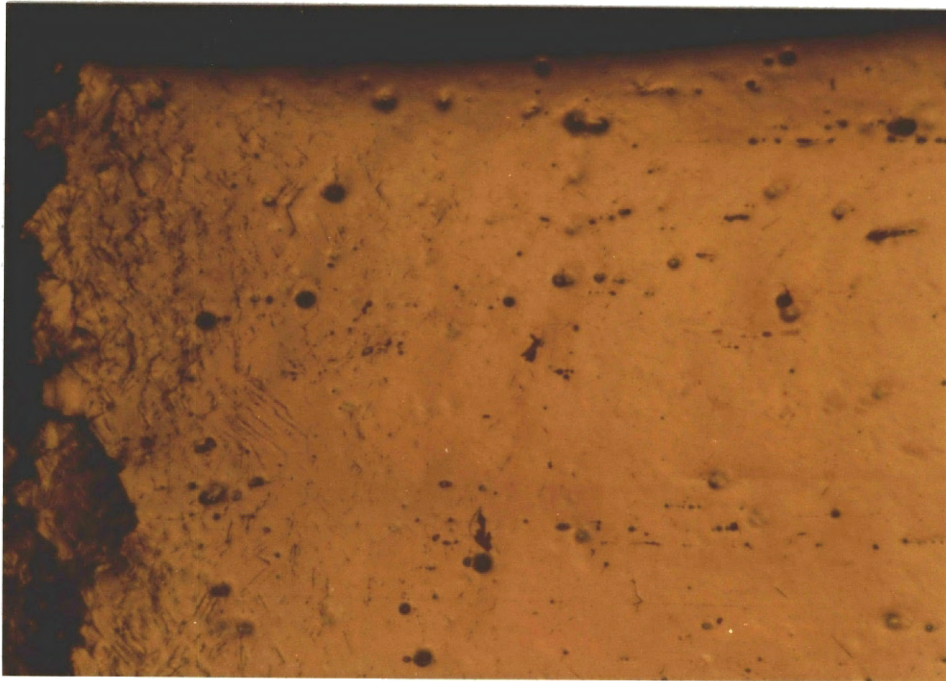
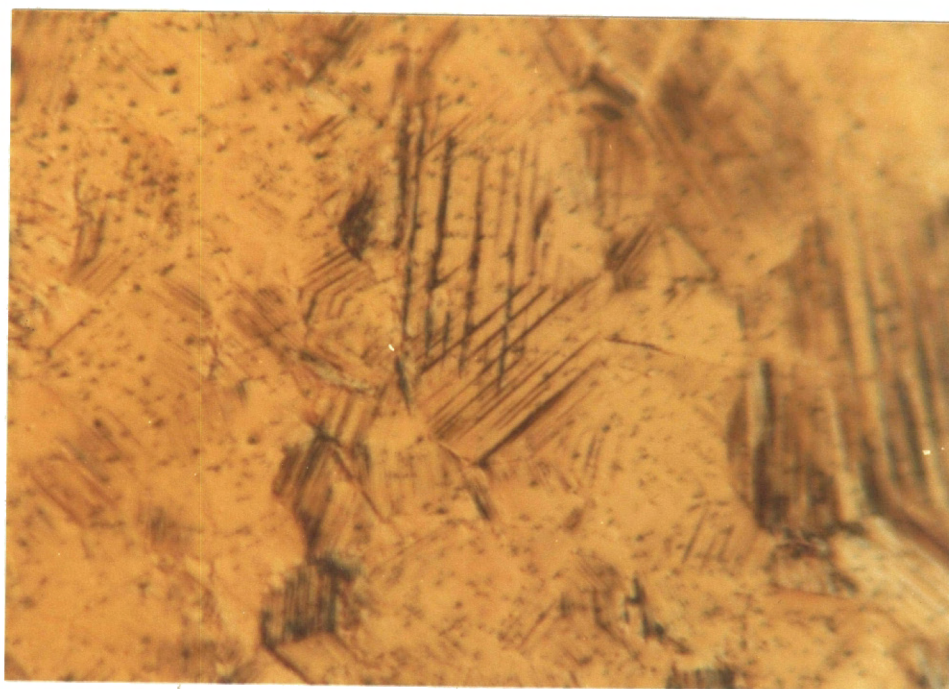
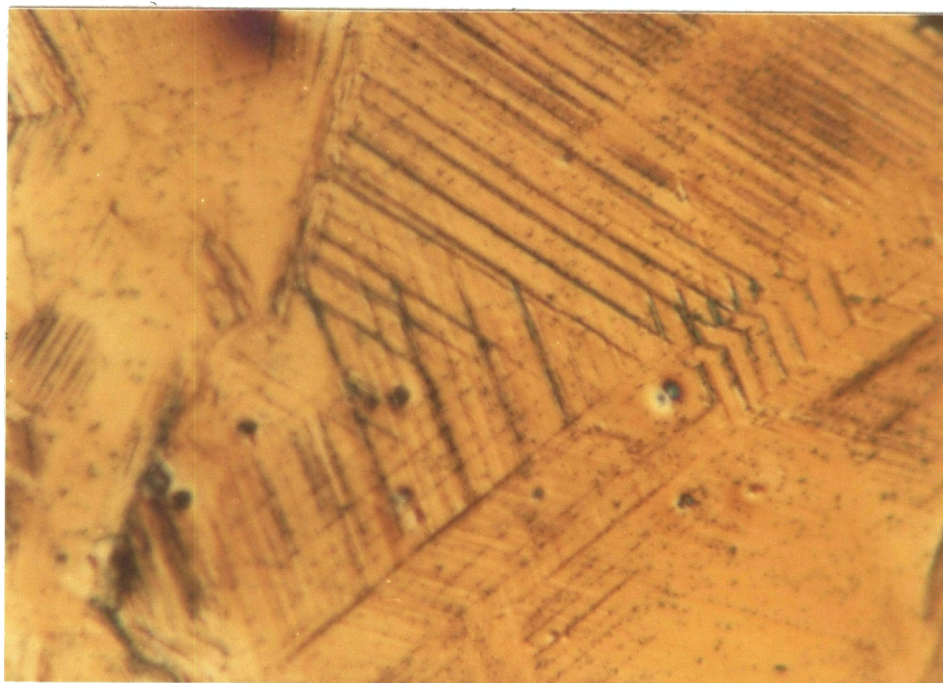


Figure 18. Triplex Slip Illustrating the Multiplicity of Slip Systems Activated in LCF. Specimen number 12, SHT, D = 24.2 mm,  $N_f = 10,300$  (x 780).

Figure 19. Duplex Slip with Pronounced Vertical Slip Bands Oriented Parallel to the Fracture Edge. Specimen number 26, OVA, D = 34.7 mm,  $N_f = 4,040$  (x 780).



The surfaces of 12 specimens were examined very closely with the optical microscope. Using the diameter of the field of vision as a measuring reference, cracking was discovered to be predominantly intergranular. With solution heat treated and overaged specimens, transgranular cracking accounted for less than 20 percent of the total. Optimum aged specimens were cracked intergranularly approximately 60 percent for low cycle fatigue and 80 percent for high cycle fatigue. The two modes of cracking are illustrated in Figures 20 and 21.

The majority of inclusions were located at grain boundaries, Figure 22. These have been shown to be composed of titanium compounds (5, 18). Inclusions and cracks often coincided, Figure 23. In a few cases, especially in high cycle fatigue, cracks unmistakably avoided inclusions, Figure 24.

The scanning electron microscope (SEM) offers a different perspective over that of the optical microscope. Figures 25 and 26 are a comparison of the same fracture edge of an optimum aged specimen. At higher magnifications with the SEM, extrusions became evident and prominent slip bands were cracked, Figure 27. In Figure 28, slip was mostly planar with perhaps local regions of wavy slip. Cracks often propagated through regions of dense slip band formation despite their intergranular nature, Figures 29 through 32. Ductile tearing was also observed. In Figure 33, a single transgranular crack formed as opposed to the multiple cracks of Figure 27. A second phase particle of Figure 34 is the site of an intergranular crack.

The orders of magnitude greater depth of focus of the SEM allowed fracture surfaces to be monitored. In Figure 35, a considerable amount of secondary cracking has developed. Striations were coarse, charac-

Figure 20. Longitudinal and Transverse Slip Band Cracking Occurring Adjacent to Intergranular Cracking. Crack oriented parallel to fracture edge. Specimen number 35, OA, D = 37.1 mm,  $N_f = 24,000$  (x 780).

Figure 21. The Same Specimen as Shown in Figure 20 with Typical Mixed Mode Cracking. The intergranular mode comprises the majority observed. Crack oriented parallel to fracture edge. Specimen number 35, OA, D = 37.1 mm,  $N_f = 24,000$  (x 385).

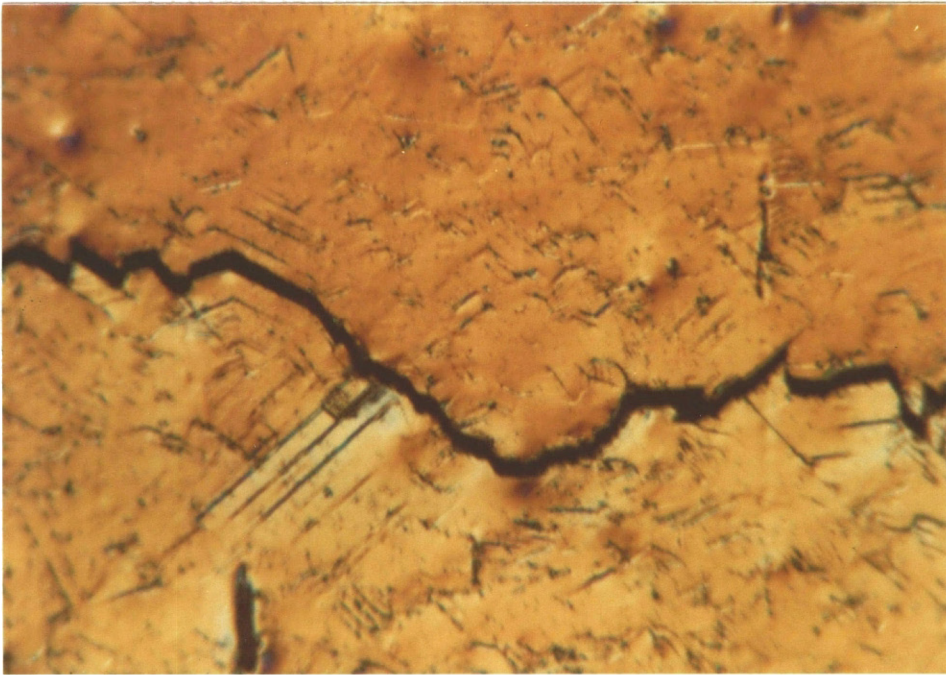
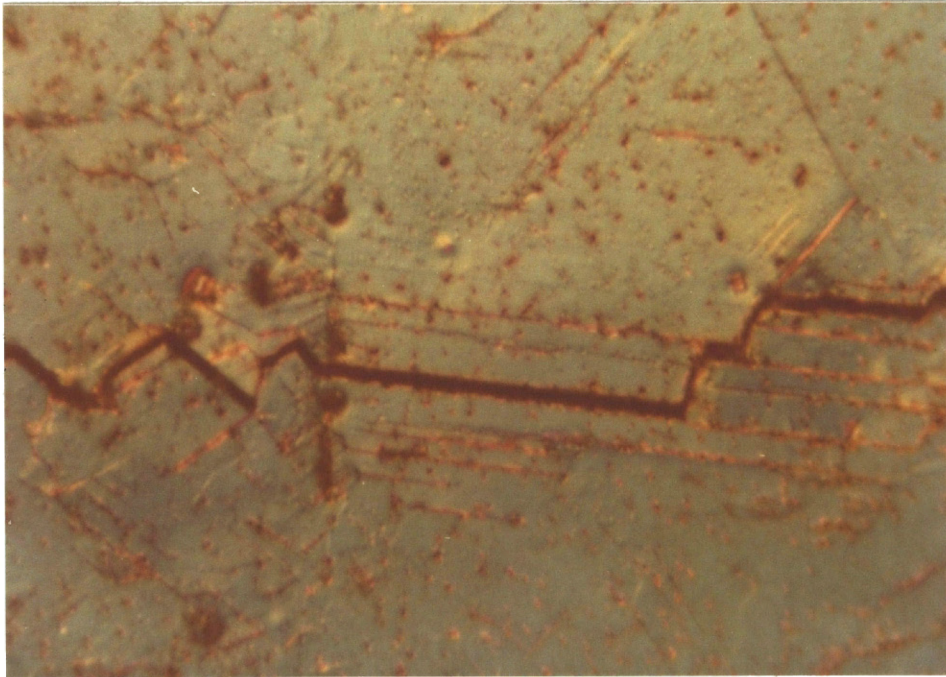


Figure 22. Fatigued and Then Etched Surface Marked by Existence of Inclusions, Slip Lines, and Cracks. Note that annealing twins are evidence of prior cold work. Grain size is 8.5. Specimen number 9, SHT, D = 15.3 mm,  $N_f = 253,400$  (x 195).

Figure 23. Intergranular Cracking Through Inclusions Located at Grain Boundaries. Specimen number 35, OA, D = 37.1 mm,  $N_f = 24,000$  (x 780).

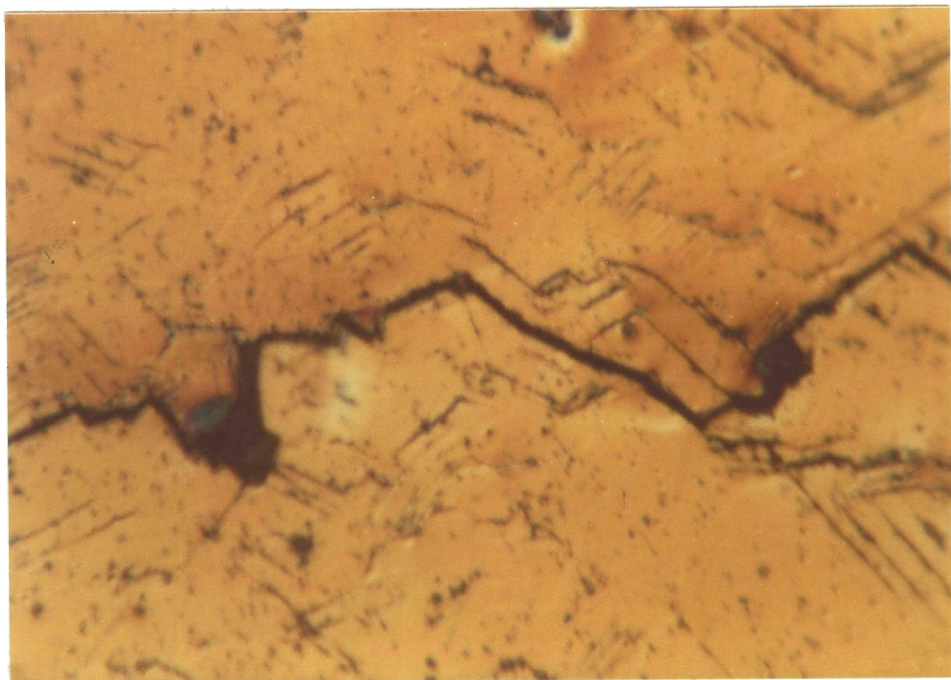
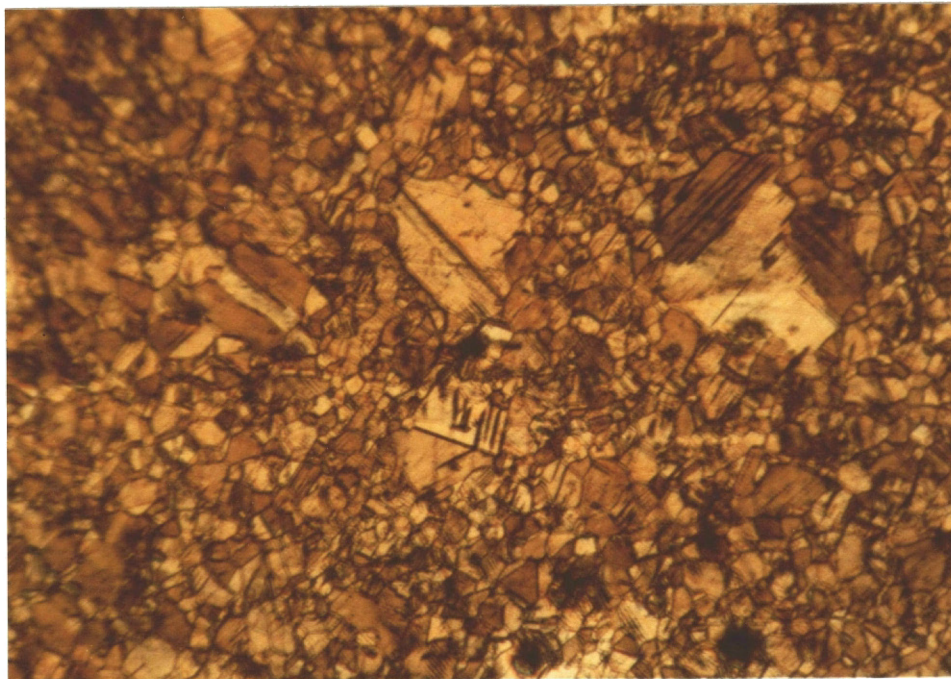


Figure 24. Intergranular Crack Adjacent to an Inclusion. Straight terminated end of crack is actually a twin boundary. Specimen number 37, OVA,  $D = 12.2$  mm,  $N_f = 3,262,000$  (x 780).

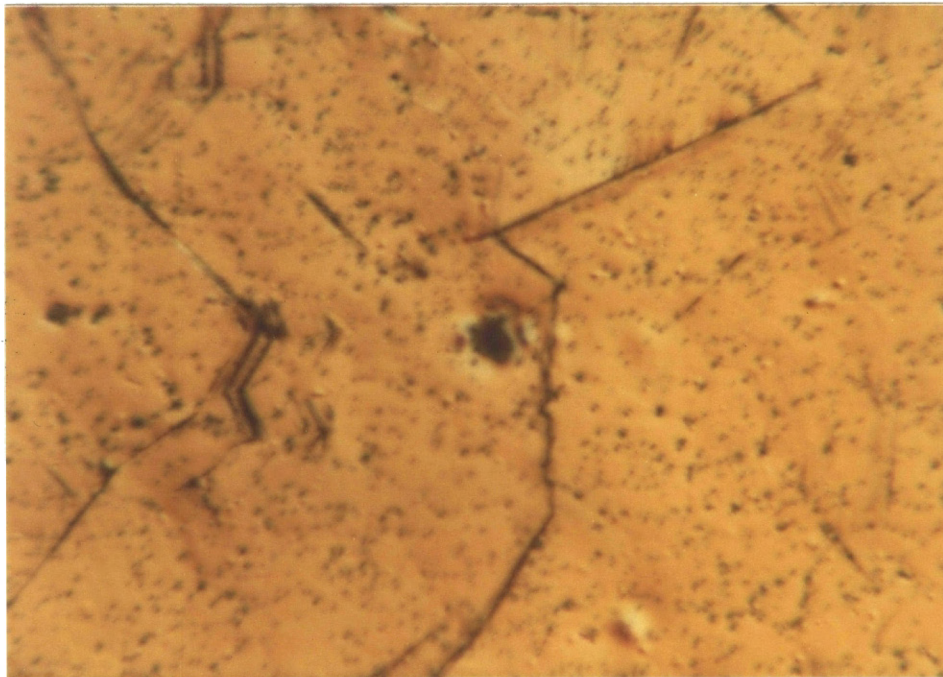


Figure 25. Group of Slip Bands Adjacent to Primary Fracture in HCF. Note primary fracture is both transgranular and intergranular. Specimen number 22, OA, D = 12.2 mm,  $N_f = 24,263,000$  (x 385).

Figure 26. SEM Photograph of the Primary Fracture of Figure 25. Note the difference of orientation from Figure 25. Specimen number 22, OA, D = 12.2 mm,  $N_f = 24,263,000$  (x 390).

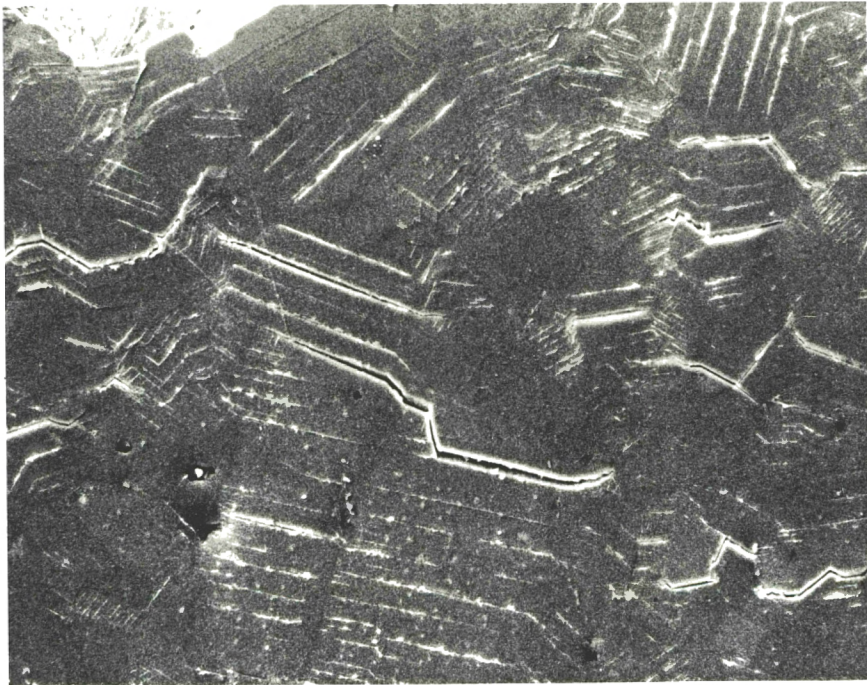
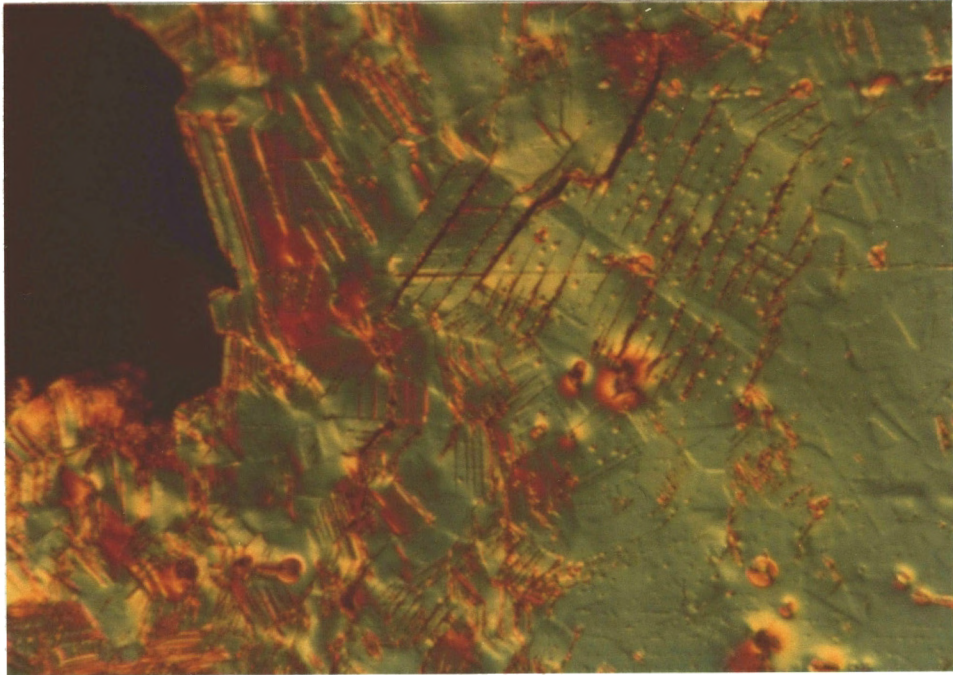


Figure 27. Extrusions and Cracks Emanating from the Prominent Slip Bands of Figures 25 and 26. Slip bands are irregularly spaced and are not uniform in length. Specimen number 22, OA, D = 12.2 mm,  $N_f = 24,263,000$  (x 3000).

Figure 28. Slip in Two Directions with Some Extrusions. Note the predominance of planar slip along the more pronounced slip direction. Specimen number 32, SHT, D = 37.1 mm,  $N_f = 3480$  (x 3000).

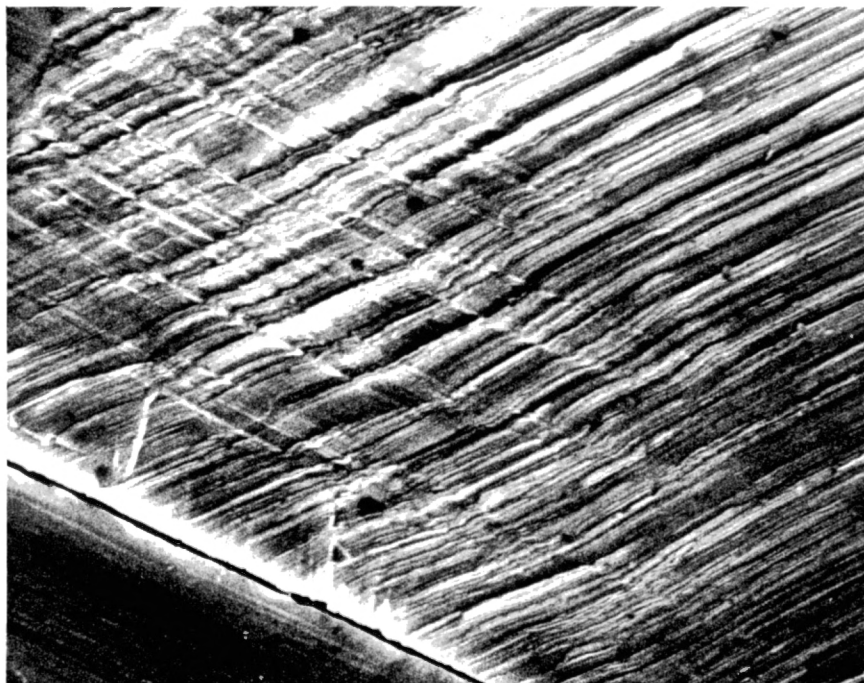
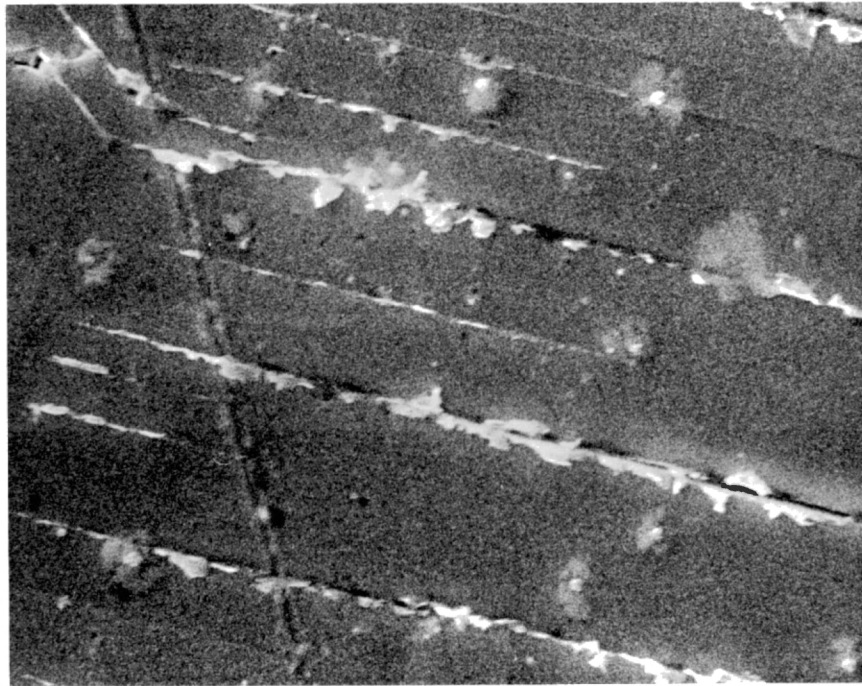


Figure 29. Mixed Mode Cracking in Areas of Concentrated Slip. Amidst much finer mixed mode cracking, intergranular cracks continue. Specimen number 13, SHT, D = 27.9 mm,  $N_f = 6,300$  (x 1300).

Figure 30. Intergranular Cracking Situated Near Regions of Dense Slip Band Formation. Gross rubbing of the surface adjacent to the fracture edge causes tearing. Specimen number 32, SHT, D = 37.1 mm,  $N_f = 3480$  (x 750).

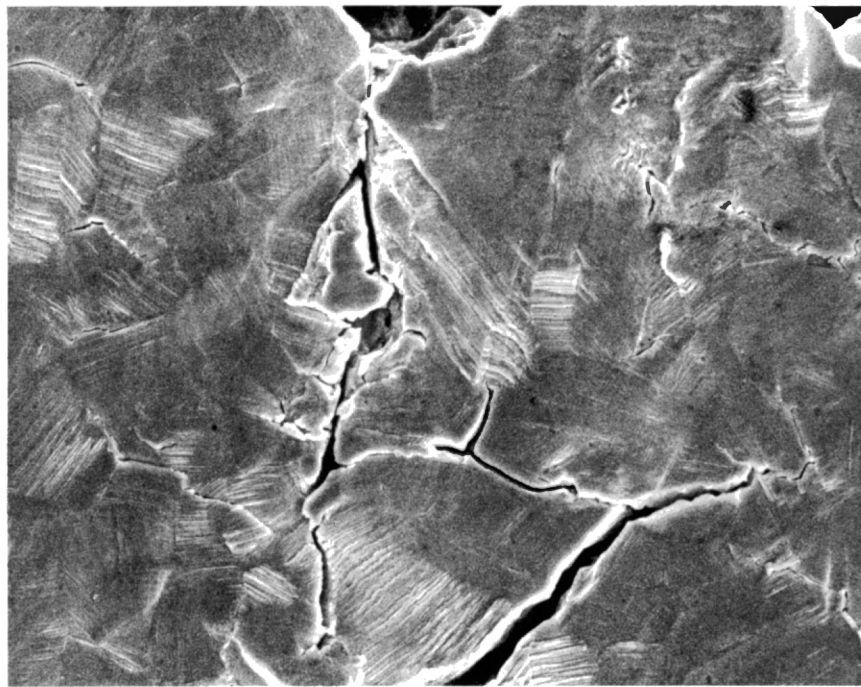
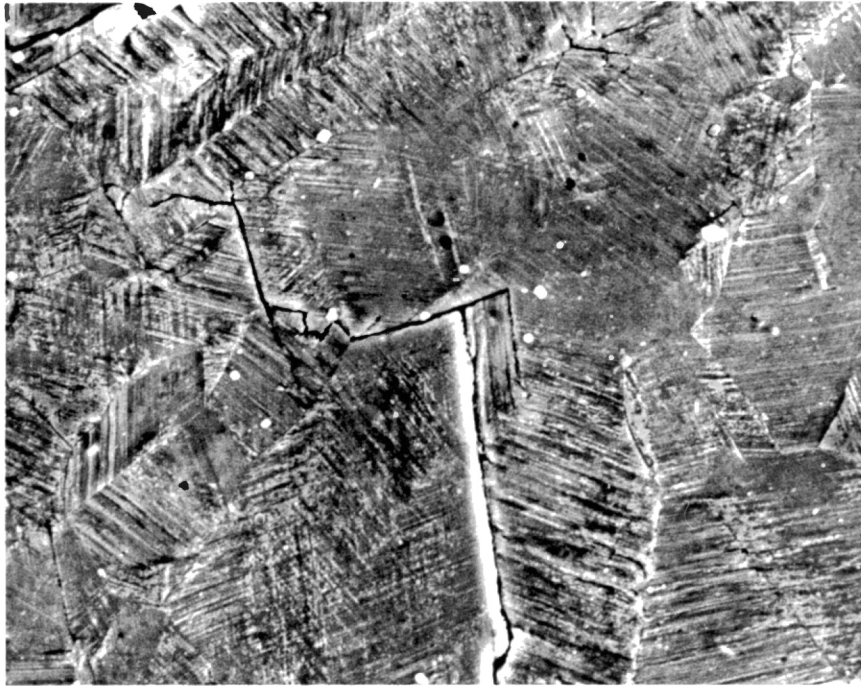


Figure 31. Local Accommodation of Stress is Achieved by Slip Band Formation and Intergranular Cracking. Specimen number 32, SHT, D = 37.1 mm,  $N_f = 3480$  (x 3000).

Figure 32. A Completely Isolated Grain Exhibiting Ductile Tearing Through Continuous Slip Lines and Twin Boundaries. High degree of deformation located near the fracture edge. Specimen number 32, SHT, D = 37.1 mm,  $N_f = 3480$  (x 3,000).

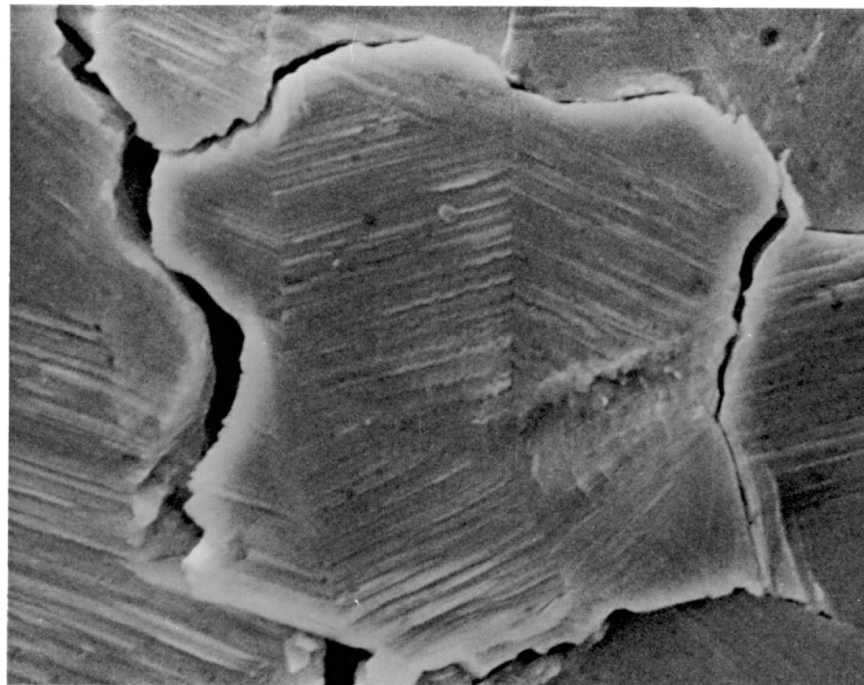
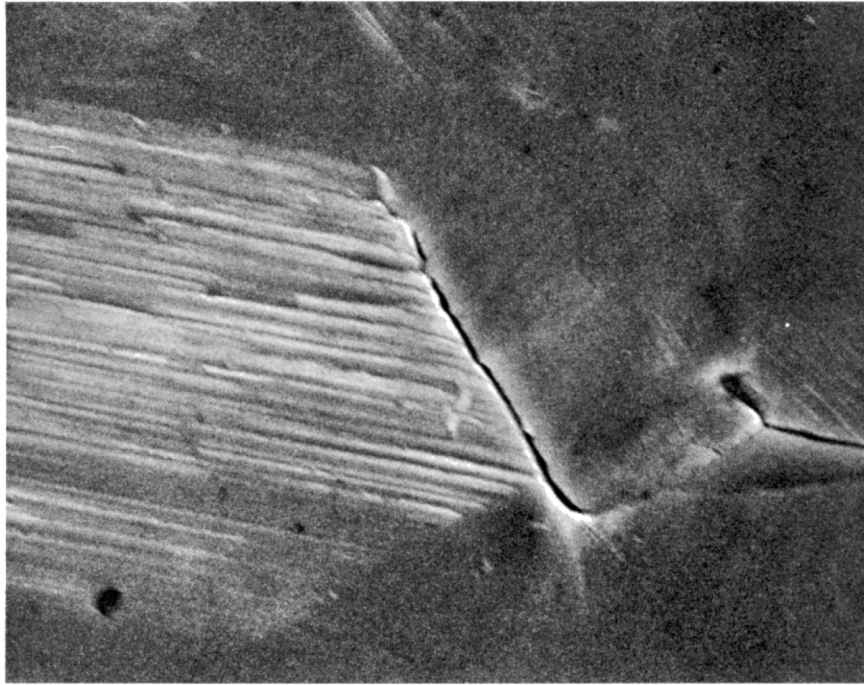


Figure 33. Duplex Slip on Both Sides of a Single Slip Band Crack That Terminates at a Cracked Grain Boundary. Specimen number 13, SHT, D = 27.9 mm,  $N_f = 6,300$  (x 9000).

Figure 34. Crack at a Second Phase Particle. Adjacent slip is minimal. Specimen number 32, SHT, D = 37.1 mm,  $N_f = 3480$  (x 10,000).

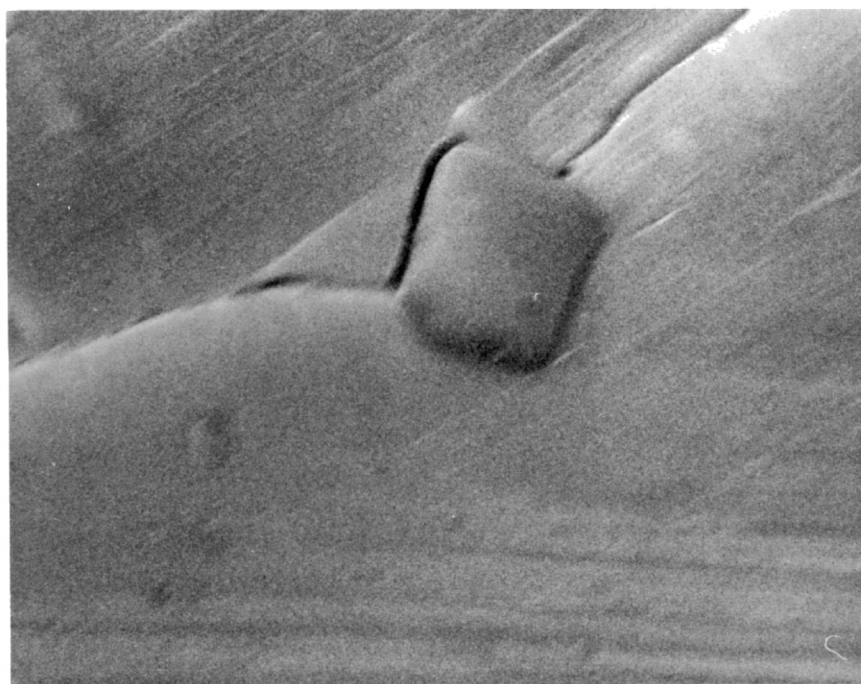
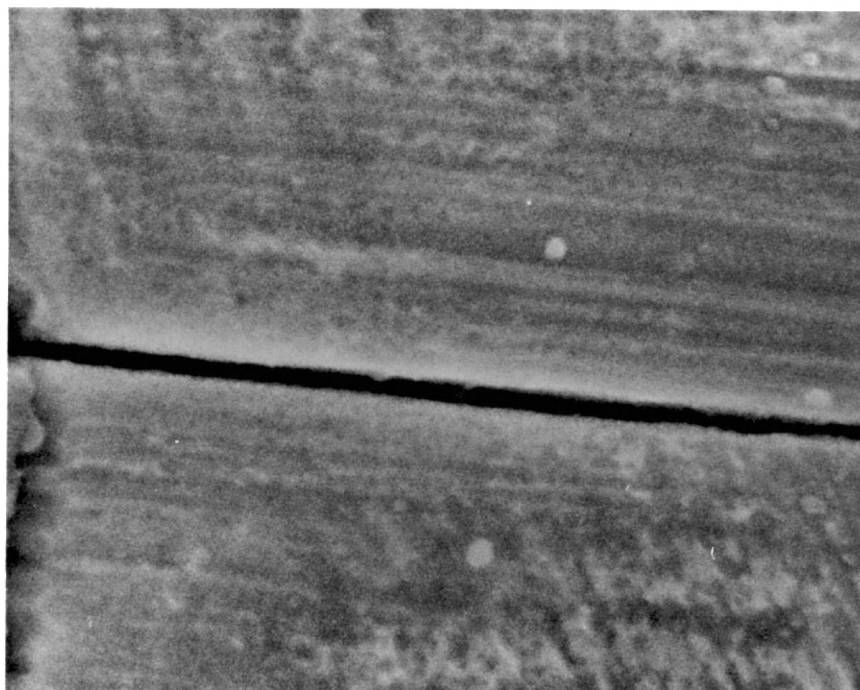
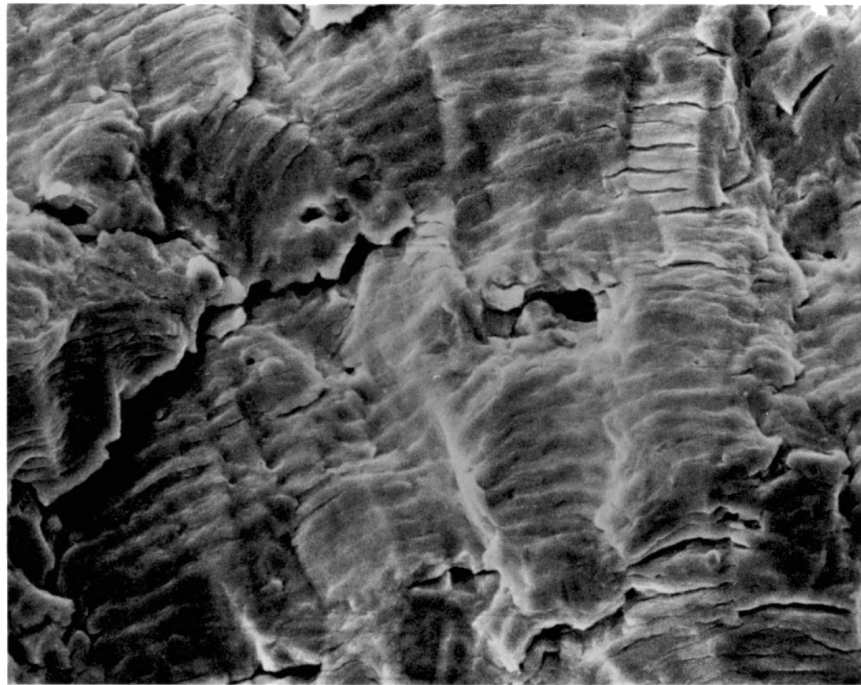


Figure 35. Considerable Amount of Secondary Cracking Amidst Coarse LCF Striations. Specimen number 31, SHT, D = 30.9 mm,  $N_f = 5,400$  (x 1500).

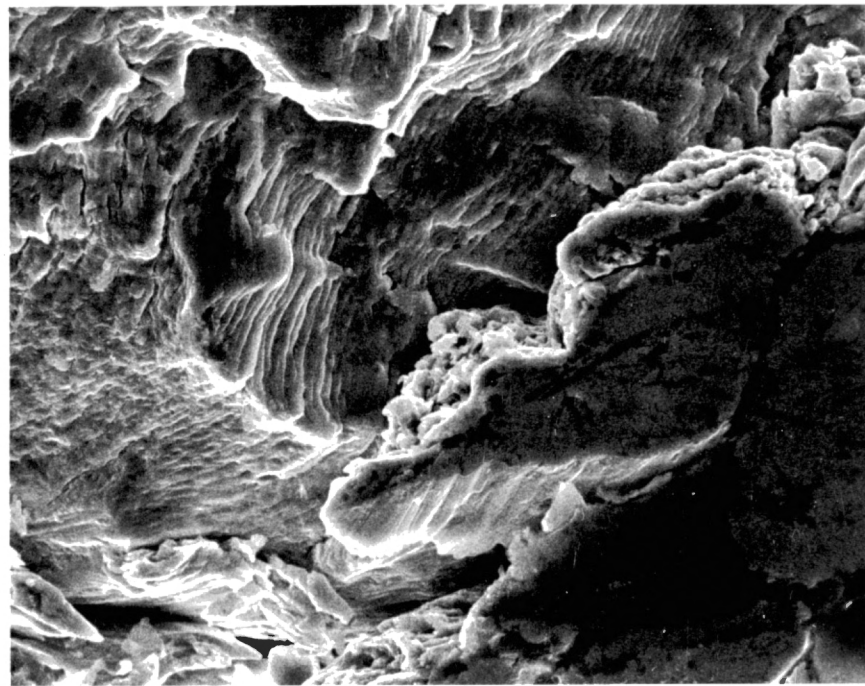
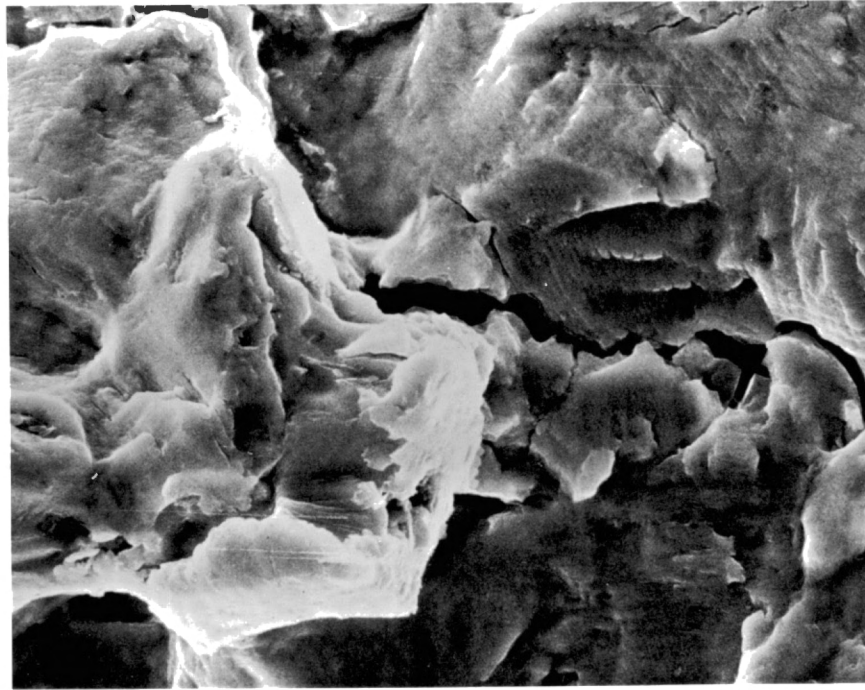


teristic of low cycle fatigue. Correspondingly, in Figure 36, secondary cracks were seen in conjunction with very fine striations formed during high cycle fatigue.

The stage I to stage II crack propagation transition in Monel K-500 was observed at different depths from the specimen surface. Typically the transition did not evolve at a unique depth, but varied from a consistent minimum depth of 10  $\mu\text{m}$  to over 100  $\mu\text{m}$ . In Figure 37, the transition was measured to be 10  $\mu\text{m}$ .

Figure 36. Secondary Cracking Associated with Fine HCF Striations in the Central Region of the Fracture Surface. Specimen number 22, OA, D = 12.2 mm,  $N_f = 24,263,000$  (x 3000).

Figure 37. Stage I to Stage II Crack Propagation Transition. Depth of transition is approximately 10  $\mu\text{m}$  measured from edge of fracture seen at the top of the photograph. Specimen number 18, OA, D = 30.9 mm,  $N_f = 29,700$  (x 3000).



## CHAPTER IV

### DISCUSSION

Over the entire spectrum of fatigue testing, optimum aged Monel K-500 exhibited superior life to that of solution heat treated or overaged material. The improvement is attributed to the strengthening mechanisms associated with the precipitation of a coherent submicroscopic  $\gamma'$  phase. The essence of the  $\gamma'$  phase was to impede dislocation motion inherent with plastic deformation. Stated in another way, the  $\gamma'$  phase increased the yield strength, thus requiring even greater levels of stress to produce the same amount of plastic deformation. Note that local plastic deformation occurs in both low and high cycle fatigue. For strain controlled low cycle fatigue, induced stresses are relatively high and significantly large plastic strains develop. It is generally believed that sufficient strain energy exists for fatigue crack initiation and stage I propagation. Hence, stage II crack propagation dominates, and accounts for the greatest proportion of life. High cycle fatigue is usually associated with relatively low induced stresses, but very localized plastic strains remain. Since strain energy is much lower, fatigue crack initiation and stage I propagation dominate.

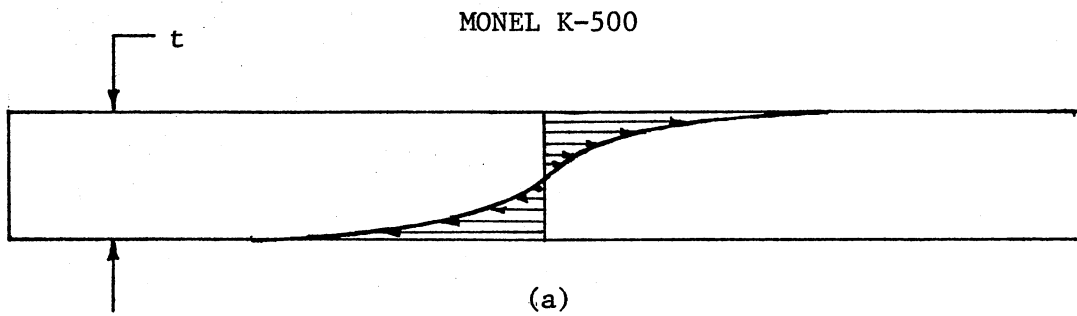
The surface hardness response to cyclic plastic deformation was expected to be proportional to the magnitude of the strain hardening exponent. This was supported by the 50 point maximum Vickers hardness

increase in solution heat treated specimens. Overaged specimens increased by a maximum of 40 points, understandably less because of its slightly lower strain hardening exponent. Optimum aged specimens did not change in hardness, a consequence of the relatively low strain hardening exponent.

In a companion study of commercially pure nickel by Fila (3), the maximum increase in Vickers hardness was approximately 100 points, corresponding to a strain hardening exponent of 0.5. However, it must be noted that Fila's specimens were 1.7 times thicker. Therefore, a less steeply sloped strain gradient would develop as a function of depth, Figure 38(b). A constant relationship between indenter weight and hardness existed for nickel above  $H_V \approx 140$  and nickel also peaked to a constant maximum of  $H_V \approx 160$ . Fila reasoned that no hardness variations with depth occurred which was in agreement with the conclusions of several other investigators.

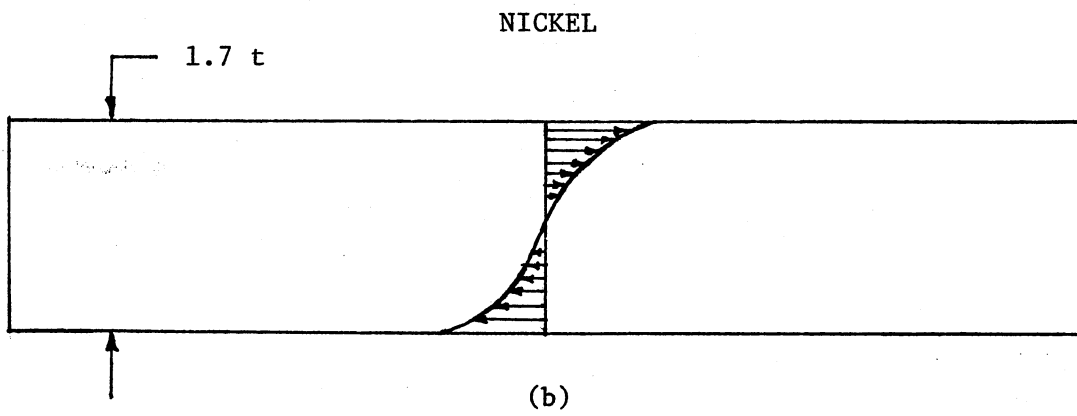
Selected solution heat treated and overaged Monel K-500 specimens were tested with two indenter weights. Unlike nickel, the 100 g weight consistently produced a higher hardness than the 500 g weight, suggesting that a hardness gradient developed. This feature could possibly be explained in terms of a dislocation substructure that decreased in intensity with depth, concurrent with the viewpoint of Kramer (12). However, it was reasoned that the more steeply sloped strain gradient characteristic of thin specimens was responsible, Figure 38(a). Kriener (13) discovered the same phenomena in Nickel 200, the identical material used by Fila. Additional justification is that the maximum hardness change as a result of fatigue was only 50 Vickers hardness points. This amount of change is hardly excessive and contradicts

Figure 38. Representative Strain Gradients for Monel K-500 and Nickel 200 as a Function of Depth.  $t$  = thickness (Not to scale.)



DEPTH  
DIRECTION

Detailed description: A vertical double-headed arrow with the word 'DEPTH' to its left and 'DIRECTION' to its right, indicating the vertical axis of the diagram.



Kramer's (12) viewpoint that a high degree of hardness should accumulate. The conclusion is that the two indenter weights were effectively detecting differences in material response to different levels of strain below the surface.

Table IV shows that for a criterion of approximately 10% slip as seen in white light, hardness varied with heat treatment and indenter weight. This did not occur in nickel, but instead hardness was always a constant value of  $H_V \approx 140$  for the same criterion (3).

The mixed mode type of cracking observed in Monel K-500 was also reported in nickel (4). Monel K-500 produced a greater proportion of intergranular cracking, however. It was proposed for Monel K-500 that the segregation of impurities to grain boundaries was partly responsible for this behavior. It must be pointed out that although fatigue crack propagation usually progressed intergranularly, initiation was believed to begin at prominent slip bands. Evidence of this can be examined in Figure 17. The higher free surface energy associated with the gauge length edges increased the stress intensity of any preexisting flaws located at that point. This, coupled with less than absolutely perfect specimen alignment, was thought to accelerate crack initiation. Isolated slip bands developed near the edge, and then cracks propagated intergranularly transverse to the gauge length. Inclusions were not crack propagation sites, but instead were often located in the crack path by virtue of their preference for grain boundaries. For example, the inclusion of Figure 24 was precipitated within a grain. As a result the nearby crack avoided the inclusion. The mode of cracking has also been found to be a function of environment. In studies by Purushothaman et al. (18) and Morris et al. (15), cracking was reported

to be primarily transgranular in vacuum, but mostly intergranular in hydrogen. Oxygen, a moderately aggressive environment, produced a slight increase in intergranular cracking.

The scanning electron microscope was instrumental in the evaluation of slip morphology. Slip bands were characterized by extrusions, similar to those seen by Fila and Price (4) with nickel. Figure 28 illustrates that slip was highly planar, although some wavy slip was discovered in regions of gross surface distortion near the fracture edge. Kriener (13) along with Fila and Price, detected mostly planar slip in their studies of nickel. According to Hertzberg (9), the proportion of planar versus wavy slip can be predicted by the magnitude of the stacking fault energy. It should be pointed out that the stacking fault energy of nickel and Monel K-500 are significantly different. In a recent study by Carter and Holmes (2), the stacking fault energy of nickel was calculated to be 120-130 erg/cm<sup>2</sup>. Karnthaler (11) reported that the stacking fault energy of nickel and copper was 120 and 41 erg/cm<sup>2</sup> respectively. Normalizing the data of Harris et al. (8), the author estimates the stacking fault energy of Monel K-500 to be 60-80 erg/cm<sup>2</sup>. The logical conclusion is that stacking fault energy by itself is not sufficient criteria for the prediction of planar or wavy slip.

Other features relevant to Monel K-500 were often similar to those observed in nickel by Fila and Price (4). Slip bands were cracked, especially those in regions of massive plastic deformation. Cracks, regardless of mode, penetrated regions of massive localized slip for both materials. This is shown in Figures 29 and 30.

The fracture surface of Monel K-500 was marked by numerous coarse

striations in solution heat treated specimens. Alternatively, it was difficult to clearly distinguish the fine striations in optimum aged specimens, especially for high cycle fatigue. Again it was believed that the magnitude of the strain hardening exponent was related to the intensity of fracture surface morphology.

The stage I to stage II crack propagation transition shown in Figure 37 was not typical of all fracture surfaces. The transition most commonly occurred at a depth of approximately 100-150  $\mu\text{m}$ . The 10  $\mu\text{m}$  minimum transition depth was assumed to be the result of localized differences in the crack propagation rate. It was hypothesized that the areas exhibiting the 10  $\mu\text{m}$  dimension were "forced" to experience the transition at shallower depths by the already well developed fatigue crack at 100-150  $\mu\text{m}$ .

Recommendations for future work include the following:

- 1) Study the effects of cumulative damage by implementing interrupted fatigue testing. An optional technique might be the replication of the fatigued surfaces for examination by the scanning and/or transmission electron microscope.
- 2) Investigate the fatigue behavior of different Ni-Cu or Cu-Ni alloys such as C71500. Other nickel alloys that could be related to this study are Incoloy, Inconel, etc.

## CHAPTER V

### CONCLUSIONS

The major conclusions of this study are summarized as follows:

1. For low and high cycle fatigue, optimum aged specimens demonstrated superior life over that of solution heat treated and overaged specimens. The superior life was attributed to the strengthening effects imparted by the  $\gamma'$  phase.
2. The quantity of fatigue damage in terms surface hardness change, amount of cracking, and slip density correlated well with the magnitude of the strain hardening exponent.
3. The surface hardness profiles for Monel K-500 were effected by heat treatment, indenter weight, cycles to failure, and specimen thickness. These features differed from those found with commercially pure nickel.
4. Cracking initiated at slip bands near gauge length edges. Propagation was in a mixed mode fashion, but with a higher proportion of intergranular cracking.
5. Slip was mostly planar in spite of the moderate value of stacking fault energy.
6. The stage I to stage II crack propagation transition occurred at a depth of approximately 100-150  $\mu\text{m}$ .

#### A SELECTED BIBLIOGRAPHY

- (1) American Society For Metals. Metals Handbook, 8th Ed., Vol. 9, Metals Park, Ohio, 1964, p. 300.
- (2) Carter, C. B., and S. M. Holmes. "The Stacking-Fault Energy of Nickel." Philosophical Magazine, Vol. 35 (1977), pp. 1161-1172.
- (3) Fila, J. A. "A Study of the Effects of Strain Amplitude and Environment on the Mechanism of Fatigue Crack Initiation in Nickel." (Unpub. M.S. thesis, Oklahoma State University, May, 1978.)
- (4) Fila, J. A., and C. E. Price. "Changes in the Surface Appearance of Nickel During Fatigue." Proc. of the 24th National SAMPE Symposium and Exhibition., Vol. 24, Book 1 (1979), pp. 90-101.
- (5) Frandsen, J. D., W. L. Morris, and H. L. Marcus. "Fatigue Crack Propagation of a Nickel-Copper Alloy in Low-Pressure Hydrogen." Hydrogen in Metals Proc. of an Int. Conf. on the Effects of Hydrogen on Materials. American Society of Metals (1974), pp. 633-643.
- (6) Grosskreutz, J. C. "The Mechanisms of Metal Fatigue (I)." Physica Status Solidi, Vol. 47 (1971), pp. 11-31.
- (7) Grosskreutz, J. C. "The Mechanisms of Metal Fatigue (II)." Physica Status Solidi, Vol. 47 (1971), pp. 359-396.
- (8) Harris, I. R., I. L. Dillamore, R. E. Smallman, and B. E. P. Beeston. "The Influence of d-band Structure on Stacking-fault Energy." Philosophical Magazine, Vol. 14 (1966), pp. 325-333.
- (9) Hertzberg, R. W. Deformation and Fracture Mechanics of Engineering Materials. New York: John Wiley & Sons, 1976.
- (10) Huntington Alloy Products Division of the International Nickel Company, Inc. Engineering Properties of Monel Alloy K-500, Technical Bulletin T-9, Huntington, West Virginia, 1965.
- (11) Karnthaler, H. P. "The Study of Glide on {001} Planes in F.C.C. Metals Deformed at Room Temperature." Philosophical Magazine, Vol. 38, No. 2 (1978), pp. 141-156.

- (12) Kramer, I. R. "A Mechanism of Fatigue Failure." Metallurgical Transactions, Vol. 5 (1974), pp. 1735-1742.
- (13) Kreiner, J. H. "A Study of Surface Zone Deterioration of Nickel Leading to Fatigue Crack Initiation in Low Cycle Fatigue." (Unpub. Ph.D. dissertation, Oklahoma State University, May, 1979.)
- (14) Mitchell, M. R. "Fundamentals of Modern Fatigue Analysis for Design." Fatigue and Microstructure, American Society for Metals, Metals Park, Ohio, 1970, pp. 385-437.
- (15) Morris, W. L., J. D. Frandsen, and H. L. Marcus. "Environmentally Induced Transitions in Fatigue Fracture Mode." ASTM STP 600, American Society for Testing and Materials, 1976, pp. 49-61.
- (16) Plumbridge, W. J., and D. A. Ryder. "The Metallography of Fatigue." Metals and Materials, (August, 1969), pp. 119-139.
- (17) Price, C. E. (Unpub. research, School of Mechanical Engineering, Oklahoma State University, 1978.)
- (18) Purushothaman, S., R. J. Richards, J. K. Tiens, and J. D. Frandsen. "Kinetics of Environmental Fatigue Crack Growth in Nickel-Copper Alloy: Part I. In Vacuum and Oxygen." Metallurgical Transactions, Vol. 9A (1978), pp. 1101-1105.
- (19) Richards, R. J., S. Purushothaman, J. K. Tien, J. D. Frandsen, and O. Buck. "Kinetics of Environmental Fatigue Crack Growth in a Nickel-Copper Alloy: Part II. In Hydrogen." Metallurgical Transactions, Vol. 9A (1978), pp. 1107-1111.
- (20) Thompson, N., and N. J. Wadsworth. "Metal Fatigue." Advances in Physics, Vol. 7 (1958), pp. 72-169.

## APPENDIX

The Budd VSP-150 fatigue machine specified in this study had been used previously by several other researchers and students. Universal concern was expressed in that the machine lacked any method of accurately determining bending displacement. Furthermore, it was estimated that the coarsely inscribed vernier used in setting the crank offset was affecting the reproducibility of fatigue tests. The disagreeable outcome of this was that fatigue data had to be reported as a function of the crank setting instead of the more customary bending displacement.

To rectify the situation, a base-plate was constructed and mounted to the bottom three legs of the fatigue machine as illustrated in Figure 2. The main part of the base-plate was formerly a 2.3 cm thick lapping plate constructed of cast iron and ground flat to within 0.013 mm/m. A 0.953 cm thick plate of austenitic stainless steel was bolted above this. The stainless steel upper plate was then ground in place to a tolerance of 0.013 mm/m. The two piece construction had two advantages:

1. The cast iron lower plate was painted, leaving the stainless steel upper plate to serve as a corrosion free surface. This also allowed the magnetic chuck of the surface grinder to hold the assembly conveniently.
2. The combined material assembly was cheaper to fabricate than other alternatives. The cast iron plate

was provided by Professor Scheihing of the School of Technology. Chrome plating was investigated, but was more expensive.

The grip blocks housed inside the vise at the fixed end of the specimen were resurfaced. Then a rigid 2.54 cm thick lathe tool, precision ground to  $\pm 0.003$  mm, was clamped evenly in the vise. This was used to align the base-plate to the fatigue machine. This procedure ensured that clamped specimens would be parallel to the base-plate to a tolerance of 0.13 mm/m. An alignment transverse to the specimen length was not performed because the specimen width was negligible relative to the dimensions of the base-plate. Total indicated runout of the crank assembly shaft was measured to be 0.25 mm. The vice assembly was set to the height of the connecting rod clamp within 0.025 mm.

Bending displacement was defined as the linear vertical distance traversed by a point located at the center of the specimen clamping hole of Figure 1, 39, and 40. This distance was calculated as a function of vertical height from the base-plate and bend angle ( $\theta$ ). The relevant geometry is displayed in Figures 39 and 40. An analysis of the geometry resulted in the following equations.

$$MHU = A + \frac{11.72 - 11.0(1 - \cos\theta)}{\cos\theta} - (35.08 + 0.737 \tan\theta) \sin\theta$$

$$MHD = A' + \frac{11.72 - 11.0(1 - \cos\theta)}{\cos\theta} + (35.08 + 0.737 \tan\theta) \sin\theta$$

$$\text{Bending Displacement} = MHU - MHD$$

where MHU = maximum height upward (mm)

MHD = minimum height downward (mm)

The specimens of this study were used to generate a bending displacement

Figure 39. Geometry of Specimen Shown in "Maximum Height Upward"  
Position

Budd VSP-150  
Fatigue Machine

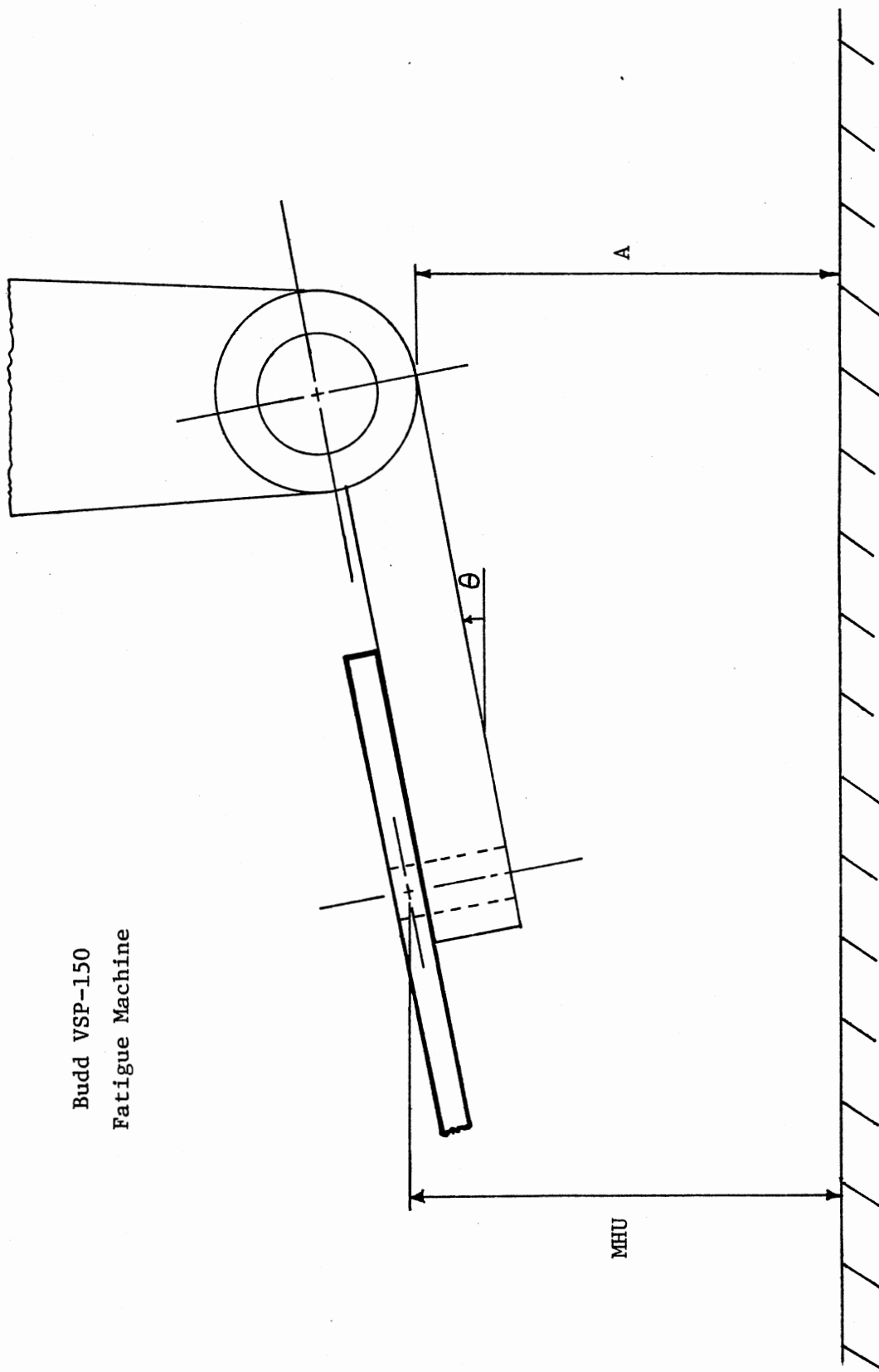
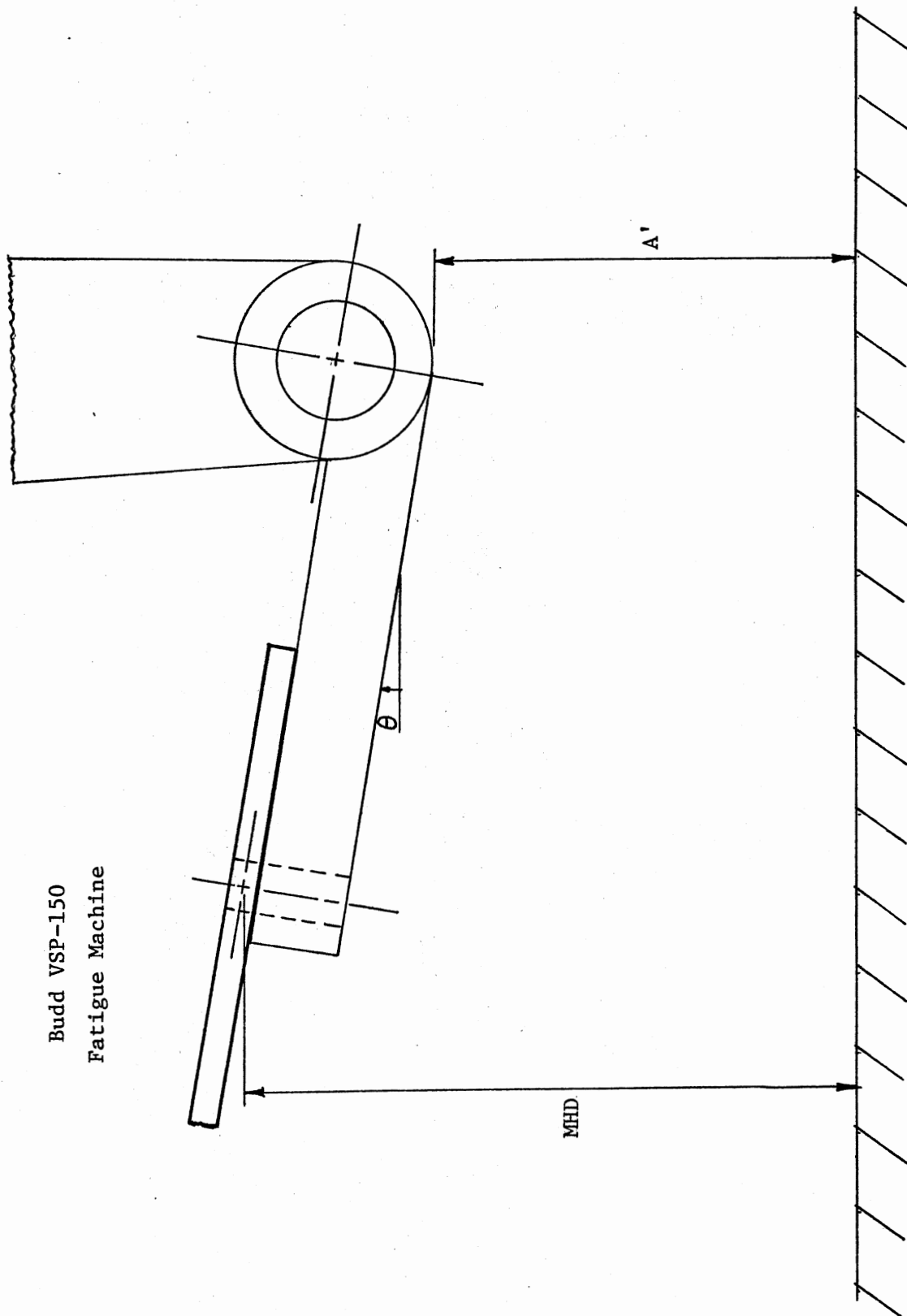


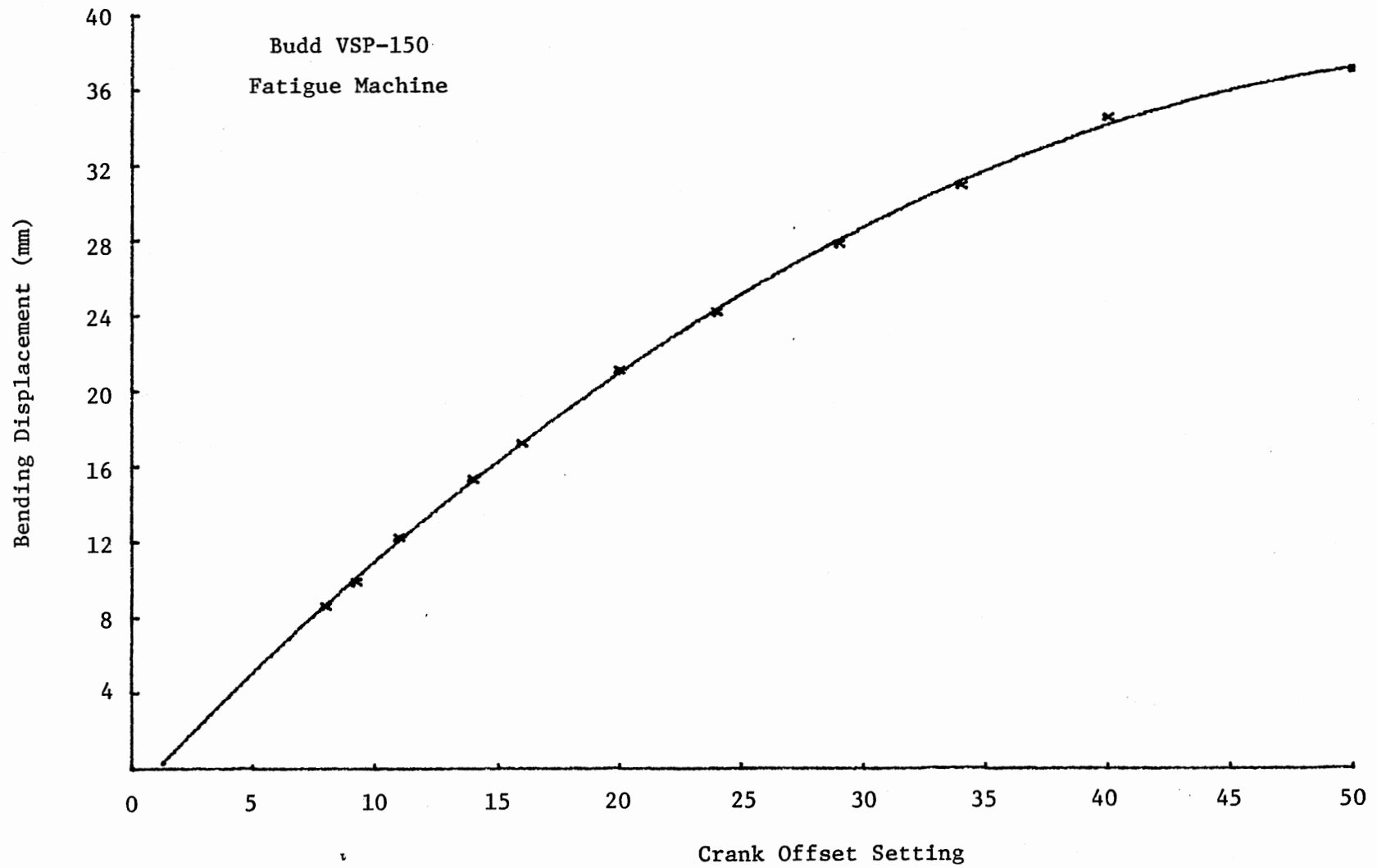
Figure 40. Geometry of Specimen Shown in "Minimum Height Downward"  
Position

Budd VSP-150  
Fatigue Machine



vs. crank setting curve, Figure 41. Once the crank setting is established, the bending displacement is accurate from this curve to a maximum tolerance of  $\pm 0.15$  mm. The author is pleased that the geometry of fracture seams had improved, with all specimens approximately symmetrical.

Figure 41. Bending Displacement as a Function of Crank Offset Setting



VITA

Gregory Wayne Henderson

Candidate for the Degree of

Master of Science

Thesis: A STUDY OF REVERSED BENDING FATIGUE ON THE NICKEL-COPPER ALLOY, MONEL K-500

Major Field: Mechanical Engineering

Biographical:

Personal Data: Born in Bridgeport, Connecticut, November 30, 1950, the son of Herschel and Marion Henderson.

Education: Graduated from Shelton High School, Shelton, Connecticut, in June, 1968; received the Bachelor of Science degree in Industrial Administration from the University of Connecticut in May, 1973; attended the University of Bridgeport on a part-time basis from September, 1973 to May, 1976; attended Oklahoma State University from January, 1977, until completion of the requirements for the Master of Science degree, December, 1979.

Professional Experience: Research assistant at Oklahoma State University, 1979; Technical assistant to Dr. C. E. Price in analyses of service failures of materials, 1979.

Professional Organizations: American Society for Metals, Society of Automotive Engineers, American Society of Mechanical Engineers.